

Dark matter particle mass and properties and axion-like dark radiation

Zhijie (Jay) Xu,^{1*}

¹Physical and Computational Sciences Directorate, Pacific Northwest National Laboratory; Richland, WA 99354, USA

Accepted XXX. Received YYY; in original form ZZZ

ABSTRACT

Two new approaches are presented for the formation and evolution of nonlinear dark matter structures in different eras and suggest a superheavy dark matter scenario (superheavy sterile neutrino, etc.) with a critical particle mass of 10^{12}GeV . Dark matter particles of this mass can have a free streaming mass equal to the particle mass and form the smallest structure among particles of any mass. In the radiation era, large-scale structures are suppressed because of rapid expansion. However, small-scale nonlinear structures can still form and evolve via direct collisions, enabled by the kinetic energy associated with the gravity of large-scale perturbations. In the "bottom-up" approach, particles of this critical mass can form the smallest haloes of two particles as early as 10^{-6}s with a density ratio of $32\pi^2$ from the spherical collapse model. The halo mass increases rapidly to $10^8 M_\odot$ at the matter-radiation equality to allow for an early and rapid galaxy formation and to $10^{13} M_\odot$ that matches observations at $z = 0$. Halo growth eventually slows down due to the self-limiting effects of dark energy. In the "top-down" approach, the mass and energy cascades are identified for hierarchical structure formation with a scale-independent constant rate of the energy cascade $\varepsilon_u \approx 10^{-7} m^2/s^3$. The energy cascade leads to universal scaling laws on relevant scales r , that is, a two-thirds law for the kinetic energy ($v_r^2 \propto \varepsilon_u^{2/3} r^{2/3}$) and a four-thirds law for the halo inner density ($\rho_r \propto \varepsilon_u^{2/3} G^{-1} r^{-4/3}$), where G is the gravitational constant. These scaling laws can be confirmed by Illustris simulations and rotation curves. By extending these scalings down to the smallest structure scale where three constants (ε_u , \hbar and G) dominate the physics, we can estimate the particle mass $m_X = (\varepsilon_u \hbar^5 G^{-4})^{1/9} = 10^{12}\text{GeV}$ (consistent with the critical mass in the bottom-up approach), size $l_X = (\varepsilon_u^{-1} \hbar G)^{1/3} = 10^{-13}\text{m}$, and a characteristic time $\tau_X = c^2/\varepsilon_u = 10^{16}\text{years}$. Here, \hbar is the Planck constant, and c is the speed of light. The binding energy of two-particle haloes $E_X = (\varepsilon_u^5 \hbar^7 G^{-2})^{1/9} = 10^{-9}\text{eV}$ suggests a dark radiation field associated with the formation and evolution of haloes. If exists, axion-like dark radiation should be produced around $t_X = (\varepsilon_u^{-5} \hbar^2 G^2)^{1/9} = 10^{-6}\text{s}$ (QCD phase transition) with a mass of $E_X = 10^{-9}\text{eV}$, a GUT scale decay constant 10^{16}GeV , or an effective axion-photon coupling 10^{-18}GeV^{-1} . The energy density of dark radiation is estimated to be about 1% of the CMB photons. This work suggests a heavy dark matter scenario along with a light axion-like dark radiation. Potential extensions to self-interacting dark matter are also presented.

Key words: Dark matter; Simulation; Theory;

CONTENTS

- 1 Introduction
- 2 Free streaming and critical particle mass
- 3 Spherical collapse model in radiation era
- 4 Structure formation by direct collisions
- 5 Nonlinear halo evolution in radiation era
- 6 Mass and energy cascade in dark matter
- 7 Inverse mass cascade in halo mass space
- 8 Energy cascade in halo mass space
- 9 Cosmic energy evolution
- 10 Energy cascade in spherical haloes
- 11 Scaling laws and halo density profiles
- 12 Dark matter particle mass and properties
- 13 The nature of cold dark matter
- 14 Axion-like dark radiation
- 15 Self-interacting dark matter
- 16 Conclusions

1 INTRODUCTION

Numerous astronomical observations support the existence of dark matter (DM). The most striking indications come from the dynamical motions of astronomical objects. The flat rotation curves of spiral galaxies point to the existence of galactic dark matter haloes with a total mass much greater than that of luminous matter [65, 66]. Although the nature of dark matter is still unclear, the cold dark matter (CDM) hypothesis, emerging in the early 1980s [59], has quickly become a leading component in the theory of formation and evolution of cosmic structures. Incorporating CDM with the cosmological constant (Λ) representing the dark energy, the ΛCDM theory is now generally considered the "standard" model of cosmology. Recent Planck measurements of the cosmic microwave background (CMB) anisotropies conclude that the amount of dark matter is about 5.3 times that of baryonic matter based on the ΛCDM cosmology [3].

In the standard ΛCDM paradigm, dark matter is cold (nonrelativistic), collisionless, dissipationless, nonbaryonic, and barely interacts with baryonic matter except through gravity [60, 71, 39, 24]. Despite its great success in the formation and evolution of large-scale structures, there are theoretical and observational difficulties as well

* E-mail: zhijie.xu@pnnl.gov;

[61, 10, 78]. These are the so-called small-scale challenges to the Λ CDM paradigm, where predictions of cold dark matter on small scales are inconsistent with some observations. These challenges are generally known as the core-cusp problem [22, 91], the missing satellite problem [36, 51], the problem of "too big to fail" [8, 9], and the diversity problem in the shape of dwarf galaxy rotation curves [56]. Some non-cold and non-collisionless dark matter models beyond the Λ CDM framework were proposed to address these issues. Examples are warm dark matter (WDM) with a steep suppression of the power spectrum at small scales [74, 43, 75] and self-interacting dark matter (SIDM) [70, 73]. Within the standard Λ CDM cosmology, baryonic feedback mechanisms were also proposed to solve these small-scale challenges, especially the core-cusp problem [10, 17].

Whether these conflicts between Λ CDM and observations can be fully resolved by baryonic physics or require different dark matter models beyond Λ CDM is still under debate. However, the difficulty of Λ CDM on small scales certainly reflects the missing components in our current understanding. These missing components can generally be classified into two categories: 1) within the Λ CDM framework, including a better understanding of baryon physics and cold dark matter physics; 2) beyond the Λ CDM, including new dark matter models beyond CDM or even the nature of gravity (modified gravity theory, etc.). The Λ CDM model has great success in the formation and evolution of large-scale structures, the abundance of different forms of matter and energy, and its predictive power, which has already been tested against many discoveries.

Taking this into account, the first step in solving these difficulties and identifying the nature of dark matter should be to fully explore and exhaust all possible options within the Λ CDM theory (i.e., the first category). Along this line, natural questions are: Are there any missing components in our current understanding of cold dark matter within Λ CDM? If so, what are they? Can we postulate the cold dark matter particle mass and properties based on these new understandings? The answers to these questions are critical for detecting dark matter and supporting/rejecting the CDM hypothesis. Therefore, using cosmological N-body simulations and observational data, this paper proposes new understandings of cold dark matter and their impacts on the mass and properties of cold dark matter particles and structure formation and evolution within the Λ CDM paradigm.

Though the nature and properties of dark matter are still a great mystery, the leading cold dark matter candidate is often assumed to be a thermal relic, weakly interacting massive particles (WIMPs) that were in local equilibrium in the early universe [72]. These thermal relics freeze out as the reaction rate becomes comparable to the expansion rate of the universe. The self-annihilation cross-section required by the right abundance of DM is of the same order as the typical electroweak cross-section, in alignment with the supersymmetric extensions of the standard model ("WIMP miracle") [35]. The mass of thermal WIMPs ranges from a few GeV to hundreds GeV, with the unitarity argument giving an upper bound of several hundred TeV [29]. However, no conclusive signals have been detected in direct or indirect searches for thermal WIMPs in this mass range. This suggests a different thinking is required beyond the standard WIMP paradigm. The other strongly motivated dark matter candidate can be the axion particles from the Peccei–Quinn (PQ) solution to the strong CP problem. Axions satisfy two conditions of cold dark matter: a sufficient non-relativistic amount and the effectively collisionless nature [19]. In addition, the relativistic axion can also be a promising candidate for dark radiation due to its small mass and weak interaction with standard-model particles [46, 44].

In this paper, we aim to new understandings of the nonlinear structure formation and evolution in both radiation and matter eras.

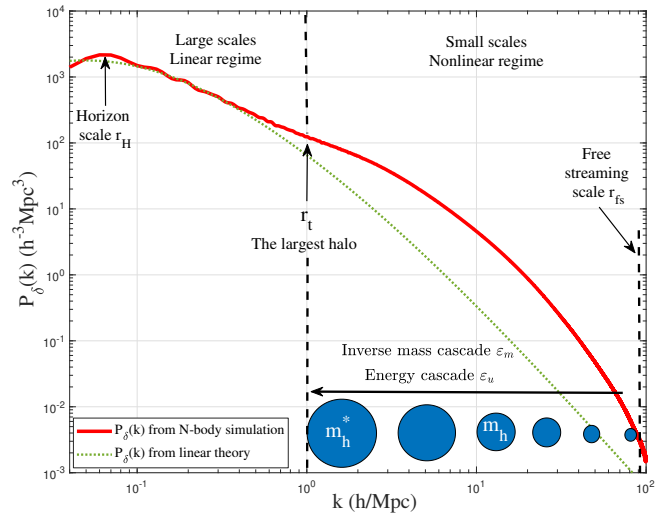


Figure 1. The variation of density power spectrum $P_\delta(k)$ with comoving wavenumber k at $z=0$. Three important scales are identified. The pivot wavenumber denotes the size of the horizon r_H at the matter-radiation equality. The scale $r_t \approx 1 \text{ Mpc}/h$ is roughly the size of the largest halo m_h^* ($z=0$). The free streaming scale r_{fs} represents the scale of the smallest nonlinear structure that can be formed as early as in the radiation era. The linear theory is in good agreement with N-body simulation on large scales $r > r_t$ (linear regime). On small scales $r < r_t$ (nonlinear regime), the linear theory does not apply and significantly underestimates the power spectrum. In this paper, we rely on analytical tools (spherical collapse model and halo-mediated mass and energy cascade) and numerical tools (N-body simulations) for nonlinear structure formation and evolution in both eras.

Based on these new findings, we postulate the possible mass and properties of cold dark matter particles. Here, we do not exclude any other dark matter models beyond the Λ CDM. Instead, we focus on the self-gravitating, cold, and collisionless particle dark matter within the Λ CDM framework that is sufficiently smooth on large scales with a fluid-like behavior. With that in mind, a complete understanding of the dynamics of dark matter flow on different scales may provide key insights into the properties of cold dark matter particles by extending these dynamics consistently down to small scales. Compared to other dark matter models, a major advantage of this approach is the consistency between dark matter particle mass and properties on small scales and the dynamics of dark matter haloes on large scales (see Fig. 25).

To facilitate the discussion, we first identify three important scales in the density spectrum of dark matter. Figure 1 presents the variation of the power spectrum with the comoving wavenumber k from N-body simulations carried out by the Virgo consortium (SCDM) [25]. The pivot wavenumber denotes the size of the horizon r_H at the matter-radiation equality. The scale r_t roughly corresponds to the size of the largest halo that separates the small scales in a non-linear regime and the large scales in a linear regime. The free streaming scale r_{fs} represents the scale of the smallest nonlinear structure that can be formed. The linear theory predictions (green dotted line from [34]) are in good agreement with N-body simulations on large scales greater than r_t . Linear perturbations on large scales are suppressed during the radiation-dominated era (Meszaros effect) and grow $\propto a$ during the matter-dominated era. However, the structure evolution on small scales smaller than r_t is highly non-linear and can only be studied by N-body simulations with the Newtonian approximation or simplified analytical tools (spherical collapse model in Section 3). The mass and energy cascade theory in this paper provides an-

other analytical approach for the nonlinear structure formation and evolution on small scales (Sections 6).

The paper is structured as follows. Sections 2 to 5 focus on a "bottom-up" approach to the nonlinear structure formation and evolution in the radiation and matter eras. Section 2 identifies a critical particle mass of 10^{12}GeV that is comparable to the particle free streaming mass. Section 3 introduces the spherical collapse model for both the matter and the radiation eras. Since the energy density of radiation significantly counteracts gravity during the radiation era, Sections 4 and 5 present the nonlinear structure formation and evolution by direct collisions. Sections 6 to 11 focus on a "top-down" approach to structure evolution. Section 6 introduces the mass and energy cascades in dark matter flow, followed by quantitative descriptions and numerical results in Sections 7 to 10. Section 11 establishes the scaling laws associated with the energy cascade that results in a halo inner density slope of $-4/3$. By extending the established scaling laws to the smallest scale, Section 12 postulates the dark matter particle mass and properties that are consistent with the structure formation and evolution in both eras. A dark radiation field is proposed to be associated with structure formation with its properties and abundance inferred in Section 14. The theory is extended to self-interacting dark matter in Section 15.

2 FREE STREAMING AND CRITICAL PARTICLE MASS

The smallest scale of dark matter haloes is sometimes called the "free-streaming" scale (Fig. 1). The thermal velocities of dark matter particles (traditionally denoted as the "X" particles) tend to erase the primordial perturbations below that scale. There are no coherent structures on scales smaller than the free streaming scale, where dark matter particles form a smooth background. In this Section, we provide a brief analysis of the free-streaming scale M_{fs} . A critical particle mass m_{Xc} is then identified that exactly equals the free streaming mass, i.e., $M_{fs}(m_{Xc}) = m_{Xc}$, which is relevant to the smallest possible dark matter structure.

The free streaming scale depends on both the mass of dark matter particles and the formation mechanism. It is usually quantified by the comoving length a particle travels before primordial perturbations start to grow significantly, which is around the time t_{eq} for matter-radiation equality. The comoving free streaming length λ_{fs} is

$$\begin{aligned} \lambda_{fs}(t) &= \int_0^{t_{eq}} \frac{\sigma_{DM}(t)}{a(t)} dt \\ &= \int_0^{t_1} \frac{\sigma_{DM}}{a} dt + \int_{t_1}^{t_2} \frac{\sigma_{DM}}{a} dt + \int_{t_2}^{t_{eq}} \frac{\sigma_{DM}}{a} dt, \end{aligned} \quad (1)$$

where $\sigma_{DM}(t)$ is the particle thermal velocity, and $a(t)$ is the scale factor. Two time scales, t_1 and t_2 , represent either the time when particles become non-relativistic (t_{NR}) or the time when particles fall out of the thermal equilibrium and decouple (freeze-out) from the background (t_{dec}), depending on the nature of dark matter. For hot relics (hot dark matter), particles become non-relativistic after decoupling ($t_{NR} > t_{dec}$) and, therefore, $t_1 = t_{dec}$ and $t_2 = t_{NR}$. For cold relics (cold dark matter), particles become non-relativistic before decoupling ($t_{NR} < t_{dec}$), such that $t_1 = t_{NR}$ and $t_2 = t_{dec}$. For the radiation era before the matter-radiation equality, the scale factor $a(t) \propto t^{1/2}$. The free streaming mass M_{fs} reads

$$M_{fs} = \frac{\pi}{6} \rho_{DM0} \lambda_{fs}^3, \quad (2)$$

where ρ_{DM0} is the dark matter density at $z = 0$.

The thermal velocity $\sigma_{DM}(t)$ also varies in different regimes:

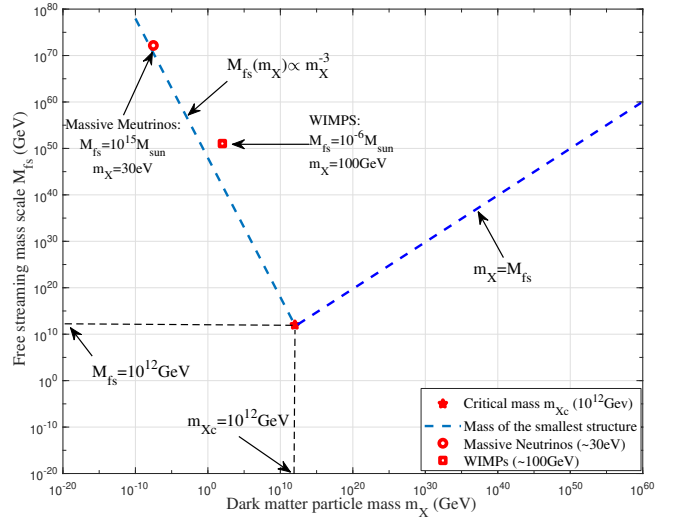


Figure 2. The free streaming mass M_{fs} decreases with the particle mass m_X . Hot massive neutrinos with a mass of 30eV can have a free streaming mass $M_{fs} \approx 10^{15} M_\odot$ (circle). For WIMP particles with a mass of 100GeV, $M_{fs} \approx 10^{-6} M_\odot$ (square). In this work, the calculated free streaming mass M_{fs} for dark matter particles of mass m_X follows the scaling $M_{fs} \propto m_X^{-3}$ (Eq. (9)). A critical particle mass m_{Xc} can be identified where $m_{Xc} = M_{fs}(m_{Xc}) \approx 10^{12}\text{GeV}$ (Eq. (10)). The dashed line plots the mass of the smallest structure (M_S) that particles of mass m_X can form. For particles with mass $m_X < m_{Xc}$, the mass of the smallest structure $M_S = M_{fs}$. For particles with mass $m_X > m_{Xc}$, $M_S = m_X$ because the free streaming mass is smaller than the particle mass, and the structure cannot be smaller than the particle itself. Therefore, $M_S = \max(M_{fs}, m_X)$. The critical mass m_{Xc} represents the mass of the smallest structure that dark matter particles of all different masses can form. Since smaller structures were formed earlier, particles of critical mass m_{Xc} also form the earliest structure (Section 4).

i) $\sigma_{DM}(t) = c$ when the particles are still relativistic ($t < t_{NR}$). During this stage, the free streaming length $\lambda_{fs} \propto a$; ii) $\sigma_{DM}(t) \propto a^{-1/2}$ when the particle becomes non-relativistic, but still coupled ($t_{NR} < t < t_{dec}$). During this stage, the free streaming length $\lambda_{fs} \propto a^{1/2}$; and iii) $\sigma_{DM}(t) \propto a^{-1}$ when the particles become non-relativistic, but also decoupled ($t > t_{dec}$ and $t > t_{NR}$). During this stage, $\lambda_{fs} \propto a^0$ is independent of time.

An alternative way of understanding the free streaming scale is via the comoving Jeans length:

$$\lambda_J(t) = \frac{\sigma_{DM}(t)}{a(t)} \sqrt{\frac{\pi}{G\bar{\rho}(t)}}, \quad (3)$$

where $\bar{\rho}(t) \propto a^{-4}$ is the background density in the radiation era. Only perturbations greater than the Jeans length will gravitationally collapse into haloes. Perturbations smaller than the Jean's length will be damped out. The variation of $\lambda_J(t)$ over time is similar to the variation of free streaming length $\lambda_{fs}(t)$.

Based on these calculations, we can estimate a free streaming mass $M_{fs} \approx 10^{15} M_\odot$ for hot massive neutrinos with a mass around 30eV. This is more likely due to the smaller particle mass, so the particles become non-relativistic much later, leading to larger free streaming length and mass. Therefore, for hot dark matter, the structure formation proceeds "top-down," which is inconsistent with observations. For WIMP particles with a much higher mass of 100GeV, the free streaming mass is around $M_{fs} \approx 10^{-6} M_\odot$ (the mass of the Earth) [5]. Cold dark matter like WIMPs takes hierarchical "bottom-up" structure formation that is in better agreement with observations. Thus, the smallest structure that can form by dark matter particles of

a given mass is radically different. The larger the particle mass m_X , the smaller the free streaming mass M_{fs} .

Figure 2 plots the decreasing M_{fs} with the particle mass m_X . There should exist a critical particle mass m_{Xc} such that M_{fs} is exactly equal to the particle mass ($M_{fs}(m_{Xc}) \equiv m_{Xc}$). Particles with a mass smaller than this critical mass m_{Xc} should form the smallest structure with a mass equal to their free streaming mass. For particles with a mass greater than m_{Xc} , its free streaming mass is smaller than the particle mass such that the smallest structure formed by these particles should have a mass equal to the particle mass. Therefore, m_{Xc} represents the mass of the smallest possible dark matter structure. Next, we will determine this critical mass m_{Xc} .

For cold dark matter particles, the non-relativistic time $t_{NR} \leq t_{dec}$. We consider the free streaming length from the first term in Eq. (1) (free streaming before t_{NR}):

$$\lambda_{fs} = \int_0^{t_{NR}} \frac{c}{a(t)} dt = \frac{2ct_{NR}}{a_{NR}} = \frac{c}{H_0} \frac{a_{NR}}{\sqrt{\Omega_{rad}}}, \quad (4)$$

where a_{NR} is the scale factor when particles become non-relativistic. Here, we use the relation in the radiation era ($t \propto a^2$),

$$t = \frac{a^2}{2H_0\sqrt{\Omega_{rad}}}, \quad (5)$$

where Ω_{rad} is the mass fraction of radiation at $z = 0$. Now we determine the free streaming mass M_{fs} using Eqs. (4) and (2),

$$M_{fs} = \frac{\pi}{6} \Omega_{DM} \bar{\rho}_0 \left(\frac{c}{H_0} \frac{a_{NR}}{\sqrt{\Omega_{rad}}} \right)^3, \quad (6)$$

where Ω_{DM} is the mass fraction of dark matter at $z = 0$. The critical density of the universe is $\bar{\rho}_0 = 3H_0^2/8\pi G$. The scale factor a_{NR} also depends on the mass of the particles m_X . Dark matter particles become non-relativistic when the radiation temperature T_γ is comparable to the particle mass,

$$3k_B T_\gamma(a_{NR}) = m_{Xc}^2 \quad \text{and} \quad T_\gamma(a) = T_{\gamma 0} a^{-1}, \quad (7)$$

where the radiation temperature redshifts with time as $T_\gamma \propto a^{-1}$. Here, $T_{\gamma 0} = 2.7K$ is the radiation temperature (CMB) at $z = 0$. Solve Eq. (7), the scale factor a_{NR} should read

$$a_{NR} = \frac{3k_B T_{\gamma 0}}{m_{Xc}^2}. \quad (8)$$

Inserting a_{NR} into Eq. (6) leads to the free streaming mass

$$M_{fs} = \frac{1}{16} \left[\frac{\Omega_{DM}}{\Omega_{rad}^{3/2}} \frac{(3k_B T_{\gamma 0})^3}{GH_0 c^3} \right] m_X^{-3} \propto m_X^{-3}. \quad (9)$$

Let $M_{fs} = m_X$ leads to the critical particle mass m_{Xc} :

$$m_{Xc} = \frac{1}{2} \left[\frac{\Omega_{DM}}{\Omega_{rad}^{3/2}} \frac{(3k_B T_{\gamma 0})^3}{GH_0 c^3} \right]^{\frac{1}{3}} \approx 1.5 \times 10^{-15} \text{ kg}. \quad (10)$$

This is a very important mass scale, as we will revisit it very often.

We may also relate the critical mass m_{Xc} to quantities at the Planck scale. Radiation density decreases as a^{-4} such that

$$\Omega_{rad} \bar{\rho}_0 a_p^{-4} = \alpha_p \rho_p \quad \text{and} \quad \rho_p = c^5/(\hbar G^2), \quad (11)$$

$$T_{\gamma 0} a_p^{-1} = \beta_p T_p \quad \text{and} \quad T_p = \sqrt{\hbar c^5/(G k_B^2)},$$

where a_p is defined as the scale factor corresponding to the Planck time $t_p = \sqrt{\hbar G/c^5} = 5.4 \times 10^{-44} \text{ s}$. Here, ρ_p is the Planck density,

T_p is the Planck temperature, and α_p and β_p are two numerical factors. The scale factor a_p is related to the Planck time by Eq. (5),

$$a_p = \left(2H_0 t_p \sqrt{\Omega_{rad}} \right)^{1/2} \approx 4.76 \times 10^{-32}. \quad (12)$$

Substituting Eq. (12) into Eq. (11), we have

$$T_{\gamma 0} = \beta_p T_p \left(\frac{\Omega_{rad} \bar{\rho}_0}{\alpha_p \rho_p} \right)^{1/4}, \quad \alpha_p = \frac{3}{32\pi}, \quad \beta_p \approx \frac{2}{5}. \quad (13)$$

Now, substitute Eq. (13) into Eqs. (8) and (6), the critical particle mass m_{Xc} can be obtained as

$$m_{Xc} = \frac{1}{2} (3\beta_p)^{\frac{3}{4}} \left(\frac{3}{8\pi\alpha_p} \right)^{\frac{3}{16}} \left(\frac{\Omega_{DM}^2}{\Omega_{rad}^{3/2}} \right)^{\frac{1}{8}} M_{pl} (H_0 t_p)^{\frac{1}{8}} \quad (14)$$

$$\approx 1.5 \times 10^{-15} \text{ kg} = 0.9 \times 10^{12} \text{ GeV}.$$

Here, $M_{pl} = 2.2 \times 10^{-8} \text{ kg}$ is the Planck mass. The dark matter fraction $\Omega_{DM} = 0.12/h^2$, the radiation fraction $\Omega_{rad} = 4.2 \times 10^{-5}/h^2$, and $h = H_0/(100 \text{ km/s/Mpc})$ is the dimensionless Hubble constant. The critical mass m_{Xc} is completely determined by the mass fractions of dark matter and radiation.

By introducing a new parameter ε_u (the rate of change of specific energy with a unit of m^2/s^3), we can rewrite the particle mass as a simple function of three parameters ε_u , \hbar and G :

$$\varepsilon_u = A \left(\frac{\Omega_{DM}^2}{\Omega_{rad}^{3/2}} H_0 \right)^{\frac{9}{8}} (c^{27} \hbar G)^{\frac{1}{16}} \approx 4 \times 10^{-7} \frac{m^2}{s^3}. \quad (15)$$

$$m_{Xc} = \left(2^8 \varepsilon_u \hbar^5 G^{-4} \right)^{\frac{1}{9}},$$

where $A \approx 2.7 \times 10^{-4}$ is a constant. As we will demonstrate (Sections 8 and 10), ε_u is a key parameter that represents the rate of energy cascade in dark matter flow and determines the halo density profile (Eq. (110)). The dynamics of large-scale haloes are dominated by ε_u , which has a microscopic origin in Eq. (15).

If the X particles have a mass of $m_{Xc} = 10^{12} \text{ GeV}$, then they are created at a time around $t_{NR} = 10^{-29} \text{ s}$ (inflationary epoch) or $a_{NR} = 10^{-24}$. They can form the smallest structure among particles of any mass. Since smaller structures were formed earlier, they may also form the earliest structure. In the next section, we discuss the formation and evolution of nonlinear structures in the early universe, which can be highly dependent on the particle mass.

3 SPHERICAL COLLAPSE MODEL IN RADIATION ERA

The dark matter particle properties can be highly relevant to nonlinear structure formation on small scales with overdensity $\delta \gg 1$, which is beyond the range of the linear perturbation theory. The structure evolution in the nonlinear regime is very complicated, and, in general, we have to use numerical approaches such as N-body simulations. Very few analytical tools are available. The spherical collapse model is a useful approximate model for nonlinear structure evolution by gravity [30]. In this section, we will follow the spherical collapse model and extend it to the radiation era.

For the spherical collapse model (SCM), we consider a spherical overdensity with a fixed given mass M and size $R(t)$ that will first reach some maximum size R_{ta} at a turn-around moment and then collapse due to its self-gravity. We denote the scale factor a_{ta} at turn-around radius R_{ta} and introduce dimensionless variables:

$$\tau \equiv H_{ta} t, \quad x \equiv \frac{a}{a_{ta}}, \quad y \equiv \frac{R}{R_{ta}}, \quad (16)$$

where H_{ta} is the Hubble parameter at turn-around. The equation of motion for non-relativistic spherical overdensity reads [30]

$$\frac{d^2 R}{dt^2} = -\frac{GM}{R^2} = -\frac{4\pi}{3}\rho_{ta}R_{ta}^3\frac{G}{R^2}, \quad (17)$$

$$\rho_{ta} = \xi_{ta}\bar{\rho}_{ta} = \xi_{ta}\frac{3H_{ta}^2}{8\pi G},$$

where ξ_{ta} is the ratio between sphere density at turnaround (ρ_{ta}) to the background density $\bar{\rho}_{ta}$ at that moment.

Integrating Eq. (17) leads to a negative constant E for the specific energy of the gravitationally bounded sphere

$$E = \frac{1}{2}\left(\frac{dR}{dt}\right)^2 - \frac{GM}{R} < 0. \quad (18)$$

Using the dimensionless coordinates in Eq. (16), the equation of motion can be rewritten as (along with the boundary conditions)

$$\frac{d^2 y}{d\tau^2} = -\frac{\xi_{ta}}{2y^2}, \quad (19)$$

$$y|_{x=0} = 0 \quad \text{and} \quad \left.\frac{dy}{d\tau}\right|_{x=1} = 0,$$

where the spherical overdensity has an initial size $R(t=0) = 0$ and a vanishing velocity at its maximum size.

The relation between x and τ or (scale factor a and physical time t) depends on the cosmology, i.e. the content of matter Ω_m , radiation Ω_{rad} , dark energy Ω_Λ , and the evolution of Hubble parameter H and background density $\bar{\rho}$, such that

$$H = H_0\sqrt{\Omega_m a^{-3} + \Omega_{rad} a^{-4} + \Omega_\Lambda} \quad \text{and} \quad \bar{\rho} = \frac{3H^2}{8\pi G}. \quad (20)$$

In Λ CDM cosmology, x and τ are related as

$$\frac{dx}{d\tau} = x\sqrt{\frac{\Omega_m a_{ta}^{-3} x^{-3} + \Omega_{rad} a_{ta}^{-4} x^{-4} + \Omega_\Lambda}{\Omega_m a_{ta}^{-3} + \Omega_{rad} a_{ta}^{-4} + \Omega_\Lambda}}. \quad (21)$$

The analytical solution of Eq. (19) can be obtained as

$$\begin{aligned} \tau &= \frac{1}{\sqrt{\xi_{ta}}} \text{acot} \left(\sqrt{\frac{1}{y} - 1} \right) - \frac{y}{\sqrt{\xi_{ta}}} \sqrt{\frac{1}{y} - 1} \\ &= \int_0^x \frac{1}{x} \sqrt{\frac{\Omega_m a_{ta}^{-3} + \Omega_{rad} a_{ta}^{-4} + \Omega_\Lambda}{\Omega_m a_{ta}^{-3} x^{-3} + \Omega_{rad} a_{ta}^{-4} x^{-4} + \Omega_\Lambda}} dx. \end{aligned} \quad (22)$$

At turnaround $y \equiv x \equiv 1$, we should have the dimensionless time

$$\tau(y=1) = \frac{\pi}{2\sqrt{\xi_{ta}}} \equiv \tau(x=1). \quad (23)$$

From the analytical solution in Eq. (22), the time derivative (or the velocity term) can be obtained as

$$\frac{dy}{d\tau} = \sqrt{\xi_{ta}} \sqrt{\frac{1}{y} - 1}. \quad (24)$$

Substituting the time derivative into the equation for the specific energy E (Eq. (18)), the turn-around time and turn-around size are

$$t_{ta} = \pi \frac{GM}{(2|E|)^{3/2}} \quad \text{and} \quad R_{ta} = \frac{GM}{|E|}, \quad (25)$$

where both the turn-around time t_{ta} and sphere size R_{ta} are proportional to the shell mass M , i.e., the larger mass scales collapse at a later time that is consistent with the hierarchical structure formation.

We first consider the matter-dominant universe with $\Omega_{rad} = \Omega_\Lambda = 0$. From Eqs. (22) and (23), the critical density ratio at turn-around

$$\tau_{ta} = \tau(x=1) = \frac{2}{3} \quad \text{and} \quad \xi_{ta} = \left(\frac{3\pi}{4}\right)^2 \approx 5.55. \quad (26)$$

Now, we can find the corresponding linear overdensity $\delta = \rho/\bar{\rho} - 1$. The ratio between sphere density $\rho(t)$ and turnaround density ρ_{ta} is (the evolution of background density $\bar{\rho} \propto a^{-3}$)

$$\frac{\rho}{\rho_{ta}} = \frac{1}{y^3}, \quad \frac{\bar{\rho}}{\bar{\rho}_{ta}} = \frac{1}{x^3}, \quad \frac{\rho/\bar{\rho}}{\rho_{ta}/\bar{\rho}_{ta}} = \frac{1+\delta}{\xi_{ta}} = \frac{x^3}{y^3}. \quad (27)$$

From this, the exact relation between variables y and x is:

$$y^3 = \left(\frac{3\pi}{4}\right)^2 \frac{x^3}{1+\delta}. \quad (28)$$

Taylor expansion of the solution in Eq. (22) leads to the linear approximation for small x and y :

$$\frac{2}{3}x^{3/2} \approx \frac{4}{3\pi} \left(\frac{2}{3}y^{3/2} + \frac{1}{5}y^{5/2} \right). \quad (29)$$

Substitute Eq. (28) into Eq. (29), we obtain the evolution of the linear overdensity $\delta^{lin} \propto a$ and the linear overdensity δ_{ta}^{lin} at turn-around,

$$\delta^{lin} = \frac{3}{5} \left(\frac{3}{4}\pi \right)^{2/3} \frac{a}{a_{ta}} \quad \text{and} \quad \delta_{ta}^{lin} = \frac{3}{5} \left(\frac{3}{4}\pi \right)^{2/3} \approx 1.06. \quad (30)$$

For fully collapsed overdensity that reaches virial equilibrium, the required time should be twice the turn-around time $t_{vir} = 2t_{ta}$ ($t \propto a^{3/2}$ in matter-dominant universe). Energy conservation requires the radius of virialized overdensity to be half the turnaround radius $R_{vir} = R_{ta}/2$, which leads to the density ratio

$$\frac{\rho_{vir}/\bar{\rho}_{vir}}{\rho_{ta}/\bar{\rho}_{ta}} = \frac{\xi_{vir}}{\xi_{ta}} = \frac{(2^{2/3})^3}{(1/2)^3} = 32. \quad (31)$$

The density ratio at virialization ξ_{vir} and the corresponding linear overdensity δ_{vir}^{lin} are

$$\xi_{vir} = 32\xi_{ta} = 18\pi^2 \quad \text{and} \quad \delta_{vir}^{lin} = 2^{2/3}\delta_{ta}^{lin} \approx 1.69. \quad (32)$$

Figure 3 summarizes the evolution of a linear overdensity δ^{lin} (solid red) in the matter era that starts from $\delta = 0$, evolves as $\delta \propto a$ in the linear regime until it reaches a value of 1.06 at the turnaround (entering the nonlinear region), and a value of 1.69 when fully virialized. The actual nonlinear overdensity δ (solid blue) can grow much faster and reach a much higher maximum ($18\pi^2 - 1$).

Next, we will extend the same model to a radiation-dominant universe with $\Omega_m = \Omega_\Lambda = 0$. In the radiation era, the energy density of radiation significantly counteracts gravity, preventing large-scale structure formation. Gravitational collapse (Eq. (17)) is only possible on very small scales where gravity exceeds expansion. This might occur because of a special phase of universe evolution before the radiation era (early matter dominant era, etc. [6]) or because of some special mechanisms leading to gravitational collapse (Section 4). At this moment, we assume that the spherical collapse can occur and seek its corresponding solutions in the radiation era.

In the radiation era, the density ratio ξ_{ta} at the turnaround can be obtained from Eqs. (21) and (23)

$$\tau_{ta} = \tau(x=1) = 1/2 \quad \text{and} \quad \xi_{ta} = \pi^2 \approx 9.87. \quad (33)$$

The ratio between sphere density $\rho(t)$, turnaround density ρ_{ta} , and background density $\bar{\rho} \propto a^{-4}$ are

$$\frac{\rho}{\rho_{ta}} = \frac{1}{y^3}, \quad \frac{\bar{\rho}}{\bar{\rho}_{ta}} = \frac{1}{x^4}, \quad \frac{\rho/\bar{\rho}}{\rho_{ta}/\bar{\rho}_{ta}} = \frac{1+\delta}{\xi_{ta}} = \frac{x^4}{y^3}. \quad (34)$$

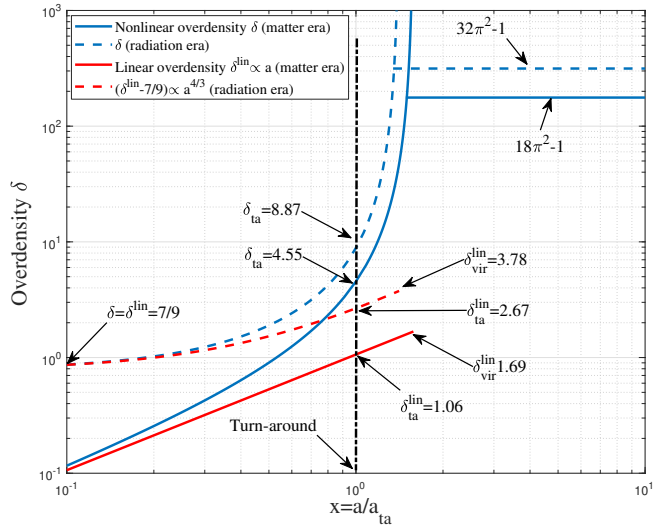


Figure 3. The evolution of overdensity (relative to the total background density) with scale factor x from a spherical collapse model for matter era and radiation era, respectively. The solid blue line plots the overdensity evolution in matter era that starts from $\delta = 0$ and reaches a maximum value of $18\pi^2 - 1$. The corresponding linear density evolves as $\delta^{lin} \propto a$ (Eq. (30)). The dashed blue line plots the overdensity evolution in the radiation era that starts from a nonzero $\delta = 7/9$ and reaches a maximum value of $32\pi^2 - 1$. The corresponding linear overdensity evolves as $(\delta^{lin} - 7/9) \propto a^{4/3}$ (Eq. (37)). In the radiation era, overdensity requires a high initial overdensity of $7/9$ and grows into a nonlinear region much later than the same overdensity in the matter era.

The exact relation between y and x now becomes

$$y^3 = \pi^2 x^4 / (1 + \delta). \quad (35)$$

Taylor expansion of Eq. (22) leads to the linear approximation:

$$\frac{1}{2}x^2 \approx \frac{1}{\pi} \left(\frac{2}{3}y^{3/2} + \frac{1}{5}y^{5/2} \right). \quad (36)$$

Using Eq. (36) and Eq. (35), we obtain the evolution of the linear overdensity and the linear overdensity at the turnaround,

$$\delta^{lin} = \frac{7}{9} + \frac{3}{5} \left(\frac{4}{3} \right)^{4/3} \pi^{2/3} \left(\frac{a}{a_{ta}} \right)^{4/3}, \quad (37)$$

$$\delta_{ta}^{lin} = \frac{7}{9} + \frac{3}{5} \left(\frac{4}{3} \right)^{4/3} \pi^{2/3} \approx 2.67.$$

For an over-density that is fully collapsed at time $t_{vir} = 2t_{ta}$ ($t \propto a^2$ for radiation era) with $R_{vir} = R_{ta}/2$, the overdensity becomes

$$\frac{\rho_{vir}/\bar{\rho}_{vir}}{\rho_{ta}/\bar{\rho}_{ta}} = \frac{\xi_{vir}}{\xi_{ta}} = \frac{(2^{1/2})^4}{(1/2)^3},$$

$$\xi_{vir} = 32\xi_{ta} = 32\pi^2, \quad (38)$$

$$\delta_{vir}^{lin} = \frac{7}{9} + \frac{3}{5} \left(\frac{4}{3} \right)^{4/3} \pi^{2/3} 2^{2/3} \approx 3.78.$$

Note that the density ratio ξ and the overdensity δ in this section refers to the ratio of the sphere density to the background density (Eq. (17)). Figure 3 also presents the evolution of a linear overdensity δ^{lin} in the radiation era that starts from an initial value $\delta = 7/9$, evolves as $\delta - 7/9 \propto a^{4/3}$ in the linear regime (Eq. (37)), until it reaches a critical value of 2.67 at the turnaround (entering the nonlinear region), and a value of 3.78 for the fully collapsed overdensity. Compared with the evolution in the matter era, we found that:

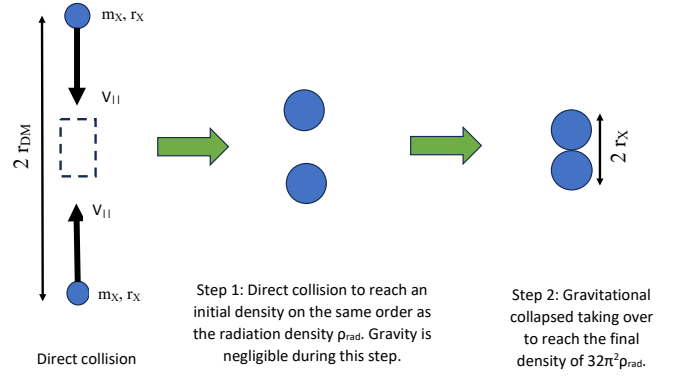


Figure 4. Two-step formation of nonlinear halo structures on small scales in the radiation era. Step 1: direct collision of two X particles of mass m_X , size r_X and a mean separation $2r_{DM}$ to reach an initial overdensity on the same order as the radiation density ρ_{rad} (Fig. 3 and Eq. (37)). The gravity is relatively weak during this step. Step 2: the gravitational collapse starts to take over to reach the final density of $32\pi^2\rho_{rad}$ (Fig. 3 and Eq. (38)).

- (i) Overdensity in the radiation era evolves into a nonlinear region much later than that in the matter era with higher linear overdensity at the turnaround (δ_{ta}^{lin}). Density ratio at turnaround ξ_{ta} and at virial equilibrium ξ_{vir} are also higher than those in the matter era.
- (ii) On small scales, the linear perturbation theory does not apply. Our solution suggests a linear overdensity $\delta^{lin} \propto 7/9 + Const \cdot a^{4/3}$.
- (iii) Gravity is weak compared to expansion in the radiation era. If gravitational collapse occurs, a special mechanism that does not involve gravity is required to give rise to the initial overdensity $\delta = 7/9$ that is comparable to the density of the radiation background. The gravitational collapse can take over subsequently. In the next section, we discuss a possible mechanism via direct collisions.

4 STRUCTURE FORMATION BY DIRECT COLLISIONS

In the radiation era, linear theory predicts a suppressed density perturbation on large scales due to fast expansion, i.e., the Meszaros effect. Perturbations on large scales are suppressed by the Hubble expansion. Therefore, large-scale structures smaller than the horizon ($r_t < r < r_H$ in Fig. 1) remain essentially frozen as a result of radiation impeding growth. However, on small scales, nonlinear structure formation and evolution are still possible in the radiation era. In this section, we discuss halo structure formation on small scales in the radiation era, while structures on large scales are still suppressed.

We begin our discussion with Fig. 4. Consider a collection of X particles with mass m_X , size r_X , and a mean separation of $2r_{DM}$. The first step is direct collisions of dark matter particles to reach an initial matter density comparable to the radiation ρ_{rad} . Gravity is not involved during this step. The second step involves the gravitational collapse of the overdensity to form virialized haloes with a final density of $32\pi^2\rho_{rad}$, as described by the spherical collapse model. During the first step of direct collision, gravity is neglected, and we focus on the collision time. For particles of size r_X , the cross-section is $\sigma_d = \pi r_X^2$. With the mean separation $r_{DM} = (3m_X/4\pi\rho_{DM})^{1/3}$, the mean free path λ_{DM} and the collision time τ_{dc} are:

$$\lambda_{DM} = \frac{m_X}{\rho_{DM}\sigma_d} = \frac{4}{3} \left(\frac{r_{DM}}{r_X} \right)^2 r_{DM},$$

$$\tau_{dc} = \frac{\lambda_{DM}}{V_{||}} = \frac{4}{3} \left(\frac{r_{DM}}{r_X} \right)^2 \frac{r_{DM}}{V_{||}}. \quad (39)$$

Obviously, $\tau_{dc} \propto a^3$ rapidly increases with time due to the expansion $r_{DM} \propto a$ for a fixed particle size r_X such that direct collision is only possible in radiation era. To calculate the time scale τ_{dc} , we need to determine the velocity $V_{||}$ and size r_X , respectively.

The peculiar velocity of the particle can be decomposed into a parallel component $V_{||}$ due to the gravity of density perturbations on large scales and a perpendicular component V_{\perp} not induced by gravity. For the perpendicular component, the comoving velocity $\mathbf{u}_{\perp} = V_{\perp}/a$ satisfies $\dot{\mathbf{u}}_{\perp} + 2H\mathbf{u}_{\perp} = 0$, so it decays rapidly as $\mathbf{u}_{\perp} \propto a^{-2}$ and $V_{\perp} \propto a^{-1}$. This is the thermal velocity that contributes to the vorticity and decays rapidly over time compared to $V_{||}$ (Fig. 5). Therefore, it is generally a good approximation to treat the large-scale velocity as being curl-free with vanishing vorticity [88]. For direct collisions, we need to compute $V_{||}$ in the radiation era.

The parallel component of the comoving velocity $\mathbf{u}_{||} = V_{||}/a$ is coupled to the density perturbations δ in dark matter. The linearized perturbation equations reads

$$\dot{\delta} + \nabla \cdot \mathbf{u}_{||} = 0, \quad (\text{continuity equation})$$

$$\dot{\mathbf{u}}_{||} + 2H\mathbf{u}_{||} = -\frac{1}{a^2} \nabla \delta \Phi, \quad (\text{momentum conservation}) \quad (40)$$

$$\nabla^2 \delta \Phi = 4\pi G \rho_{DM} a^2 \delta. \quad (\text{Poisson equation})$$

The parallel component can be further expressed as the gradient of potential perturbation $\delta \Phi$, i.e. $\mathbf{u}_{||} \propto -\nabla \delta \Phi$. From Eq. (40), equations for perturbation δ and comoving velocity $\mathbf{u}_{||}$ are obtained as

$$\begin{aligned} \dot{\delta} + 2H\delta &= 4\pi G \rho_{DM} \delta, \\ \dot{\mathbf{u}}_{||} + 2H\mathbf{u}_{||} &= 4\pi G \rho_{DM} \frac{\delta}{\bar{\rho}} \mathbf{u}_{||}. \end{aligned} \quad (41)$$

This equation is valid in both radiation and matter eras, where the Hubble parameter satisfies

$$H^2 = \frac{8}{3} \pi G \rho_{DM} \left(1 + \frac{a_{eq}}{a}\right), \quad \dot{H} = -\frac{H^2}{2} \frac{3 + 4a_{eq}/a}{1 + a_{eq}/a}. \quad (42)$$

If the gravity is neglected (right-hand-side term in Eq. (41)), we found the logarithmic growth for density perturbation $\delta \propto \ln t$ in the radiation era. For both radiation and matter eras, the well-known exact solution for δ including the gravity reads [48]

$$\delta = 2B/3 + B(a/a_{eq}), \quad (43)$$

where B is a constant. We, therefore, find that in the radiation era with $a \ll a_{eq}$, the dark matter perturbations do not grow in the linear regime, i.e., the Meszaros effect. In the matter era with $a \gg a_{eq}$, linear perturbations grow as $\propto a$. Substitute this solution into the equation for $\mathbf{u}_{||}$ in Eq. (41), we obtain an exact solution for $\mathbf{u}_{||}$

$$\begin{aligned} \mathbf{u}_{||}^2 &= C(1/a + 1/a_{eq})/a, \\ V_{||}^2 &= \mathbf{u}_{||}^2 a^2 = C(1 + a/a_{eq}), \end{aligned} \quad (44)$$

where C is a constant. Therefore, on large scales, there exists a nonzero constant velocity dispersion $V_{||}^2 = C$ associated with the frozen density perturbations δ in the radiation era. This gravity-induced velocity $V_{||}$ leads to the direct collision of dark matter particles in the early universe. In the matter era, the velocity dispersion $V_{||}^2 \propto a$ increases with time from Eq. (44). With $V_{||}$ on the order of 450 km/s at the current epoch ($a = 1$ from the Illustris simulations in Fig. 18), we estimate the constant $C = 6 \times 10^7 \text{m}^2/\text{s}^2$ such that $V_{||} \approx 7.7 \text{ km/s}$ in the radiation era. The velocity $V_{||}$ is independent of the particle mass m_X and time t (Fig. 5) and should also be independent of the dark matter particle model.

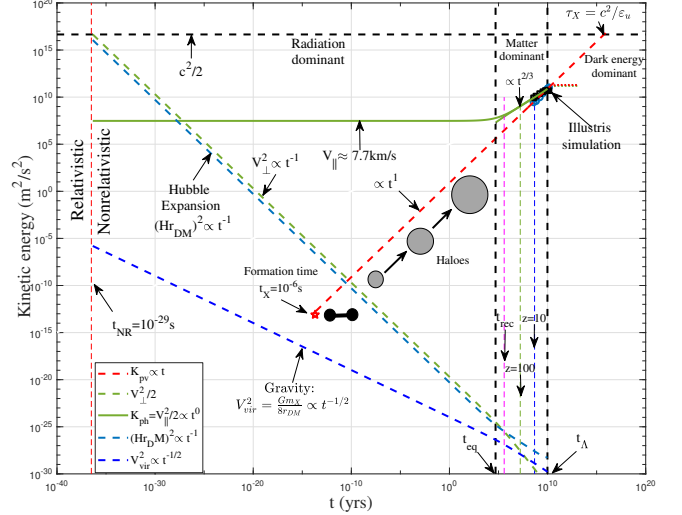


Figure 5. The evolution of kinetic energy of different velocities in the radiation era for X particles with a mass of $m_{Xc} = 10^{12} \text{ GeV}$. The effect of gravity is weak in the radiation era such that the virial velocity V_{vir} is much smaller than other velocities (dashed blue). The perpendicular component V_{\perp} (thermal velocity) and V_H (due to expansion) decreases rapidly with time (Eq. (45)). The large-scale parallel velocity $K_{ph} = V_{||}^2/2$ is due to gravity on large scales and is independent of particle mass and time. Direct collision due to velocity $V_{||}$ leads to the formation of the smallest two-particle halo at around 10^{-6} s (red star from Eq. (55)) and halo evolution in the radiation era (Section 5). The kinetic energy $K_{pv} \propto t$ on small scales ($< m_h^*$) is due to the virialization in haloes and plotted as a red dashed line (Eqs. (86) and (87)). The nature of K_{ph} and K_{pv} on large and small scales is discussed in Fig. 12. The evolution of kinetic energy in the matter era (symbols from Illustris simulation) is discussed in Fig. 18.

For comparison, we also calculated the perpendicular velocity V_{\perp} , Hubble flow V_H , and virial velocity V_{vir} due to gravity,

$$\begin{aligned} V_{\perp} &= \frac{a_{NR}}{a} c = \frac{3k_B T \gamma_0}{cm_X} a^{-1} \propto m_X^{-1} a^{-1}, \\ V_H &= Hr_{DM} \propto m_X^{1/3} a^{-1}, \\ V_{vir}^2 &= \frac{Gm_X}{8r_{DM}} \propto m_X^{2/3} a^{-1}. \end{aligned} \quad (45)$$

All of these velocities depend on both particle mass and time. Figure 5 plots the variation of different velocities in the radiation era for X particles with a mass $m_{Xc} = 10^{12} \text{ GeV}$. The virial velocity V_{vir} due to gravity is small in the radiation era when compared to the Hubble flow from expansion. The parallel peculiar velocity on large scales ($V_{||}$) is constant and independent of the particle mass m_X (solid green line). Direct collisions due to velocity $V_{||}$ led to the formation of the first non-linear structure (red star) and the evolution of structures in the radiation era. The kinetic energy on small scales increases linearly with time $K_{pv} \propto t$ due to the virialization in the haloes (red dashed line) (Eqs. (86) and (87)).

Next, we estimate the size of the particles r_X for a given particle mass m_X . Here, we consider the smallest halo structure with only two X particles. This is possible for particles with mass $m_X \geq m_{Xc}$ such that the free streaming mass M_{fs} is smaller than the particle mass m_X (Fig. 2). For particles with mass $m_X < m_{Xc}$, the free streaming mass is greater than the particle mass. The size and formation time of the smallest structure is determined by the free streaming mass M_{fs} . This is discussed separately in Section 11 (Table 3).

Now consider the smallest haloes with two X particles of mass

m_X and separation l_X , formed in virial equilibrium at time t_X ,

$$2v_X^2 = \frac{Gm_X}{l_X}, \rho_X = \frac{2m_X}{\frac{4}{3}\pi l_X^3} = \xi \bar{\rho}(t_X), H(t_X)^2 = \frac{8}{3}\pi G \bar{\rho}(t_X), \quad (46)$$

where $\bar{\rho}(t_X)$ is the background density at the formation time t_X , v_X is the virial velocity. According to the spherical collapse model, at the formation time t_X , the density of the smallest structure should be $\rho_X(t_X) = \xi \bar{\rho}(t_X)$. For the radiation era and the matter era, the density ratio $\xi = 32\pi^2$ or $18\pi^2$, respectively. The formation time t_X can be obtained from Eq. (46) as

$$t_X = \pi \frac{l_X}{v_X}. \quad (47)$$

Next, we consider the smallest possible t_X , i.e., the earliest time the two-particle haloes can form. The density of the smallest structure (ρ_X of two-particle haloes) at the earliest time of formation (the smallest t_X) should be the highest density that these structures can have. According to the "uncertainty principle," the two X particles cannot collapse to an infinite density, and there exists a maximum density. From the uncertainty principle ($\Delta p \Delta x \sim \hbar$),

$$m_X v_X \cdot r_X = n\hbar, \quad (48)$$

where \hbar is Planck constant and n is the quantum number with $n = 1$ for the ground state. Similarly, as electrons cannot be fully pulled into the nucleus due to the uncertainty principle, two X particles cannot be fully pulled into each other by gravity for the same reason, i.e., the size $r_X = l_X/2$ cannot be zero. Therefore, the momentum $m_X v_X$ and the position r_X should satisfy the uncertainty principle in Eq. (48). Combined with Eq. (46) for virial theorem, the particle size and the virial velocity are

$$r_X = l_X/2 = \frac{4\hbar^2}{G(m_X)^3} \quad \text{and} \quad v_X = \frac{G(m_X)^2}{4\hbar}. \quad (49)$$

The earliest formation time t_X that gives the highest density and also the right ratio ($\xi = 32\pi^2$ for the radiation era) is (from Eq. (47))

$$t_X(m_X) = \pi \frac{l_X}{v_X} = \frac{32\pi\hbar^3}{G^2(m_X)^5} \quad \text{for} \quad m_X \geq m_{Xc} = 10^{12} \text{ GeV}. \quad (50)$$

This equation is only valid for particles with a mass greater than the critical mass m_{Xc} such that the free streaming mass is smaller than the particle mass to allow the formation of two-particle haloes. For particles with a mass smaller than m_{Xc} , the free streaming mass can be much greater than the particle mass (Fig. 2) such that the smallest structure (haloes) formed by these particles is much larger than particles themselves. For example, the smallest halo formed by WIMPs is around $10^{-6} M_\odot$, which is much larger than WIMPs. Therefore, WIMPs cannot form two-particle haloes (Table 3).

The formation time t_X strongly decreases with particle mass m_X . Heavier particles (larger m_X) should form smaller structures (smaller r_X) at an earlier time (smaller t_X). However, this formation time t_X should also be comparable to the direct collision time scale τ_{dc} to allow a sufficient amount of time for direct collisions to occur to form these structures. With particle size r_X in Eq. (49) and velocity $V_{||}$ in Eq. (44), we are able to calculate the direct collision time scale τ_{dc} in Eq. (39) at the time of formation t_X ,

$$\tau_{dc}(m_X, t_X) = \frac{4}{3} \left(\frac{r_{DM}}{r_X} \right)^2 \frac{r_{DM}}{V_{||}}. \quad (51)$$

With all relevant quantities,

$$r_{DM}(m_X, t_X) = \left(\frac{3m_X}{4\pi\rho_{DM}} \right)^{1/3}, \quad r_X(m_X) = \frac{4\hbar^2}{G(m_X)^3}, \quad (52)$$

$$\rho_{DM}(m_X, t_X) = \frac{3H_0^2}{8\pi G} \Omega_{DM} a_X^{-3}, \quad t_X = \frac{a_X^2}{2H_0\sqrt{\Omega_{rad}}},$$

the direction collision time scale τ_{dc} can be computed as a function of particle mass m_X ,

$$\tau_{dc}(m_X) = \frac{2^8\pi^{3/2}}{3} \left(\frac{\Omega_{rad}^{3/2}}{H_0\Omega_{DM}^2} \right)^{1/2} \left(\frac{\hbar}{m_X V_{||}^2} \right)^{1/2}, \quad (53)$$

With the formation time comparable to the direct collision time or $t_X(m_X) = \tau_{dc}(m_X)$ (Eqs. (50) and (53)), the only possible particle mass m_X should read

$$m_X = \left(\frac{9}{64\pi} \frac{H_0\Omega_{DM}^2}{\Omega_{rad}^{3/2}} \frac{V_{||}^2\hbar^5}{G^4} \right)^{1/9} \approx 0.55 m_{Xc}. \quad (54)$$

Therefore, only for X particles with critical mass m_{Xc} , the direct collision time τ_{dc} is comparable to the formation time t_X , which allows the formation of the smallest two-particle haloes in the radiation era. Particles heavier than m_{Xc} will have $\tau_{dc} \gg t_X$ such that there is not sufficient time to form these structures. Particles lighter than m_{Xc} have $\tau_{dc} \ll t_X$, while the thermal velocity will prevent the formation of these two-particle haloes due to the free streaming mass greater than the particle mass (Fig. 2). Finally, only particles with a mass around m_{Xc} can form the smallest structure of two-particle haloes as described here. This is also the earliest possible structure that particles of any mass can form. The corresponding particle size, velocity, and time are as follows:

$$l_X = 2r_X = \frac{8\hbar^2}{G(m_{Xc})^3} \approx 3 \times 10^{-13} \text{ m},$$

$$v_X = \frac{G(m_{Xc})^2}{4\hbar} \approx 4 \times 10^{-7} \text{ m/s}, \quad E_X = m_{Xc} v_X^2 = 10^{-9} \text{ eV}, \quad (55)$$

$$t_X = \pi \frac{l_X}{v_X} = \frac{32\pi\hbar^3}{G^2(m_{Xc})^5} \approx 2 \times 10^{-6} \text{ s}.$$

Therefore, the smallest structure formed by two X particles of mass $m_{Xc} = 10^{12} \text{ GeV}$ has a size of 10^{-13} m , the velocity of 10^{-7} m/s and formed at around $t = 10^{-6} \text{ s}$ or $a \approx 2 \times 10^{-13}$ in the radiation era (red star in Fig. 5). We can also identify a critical energy scale $E_X = 10^{-9} \text{ eV}$ that is the binding energy in the ground state, i.e., the amount of energy released when two X particles approach from infinity to form the smallest structure. We postulate that this is also the highest energy level (with quantum number $n=1$ in Eq. (48)) of the dark radiation. The dark radiation, if exists, is produced during the formation of the earliest and smallest halo structures at the formation time 10^{-6} s (Section 14).

The key parameter ε_u that we introduced in Eq. (15) reads

$$\varepsilon_u = 2 \frac{v_X^3}{l_X} = \frac{G^4(m_{Xc}^9)}{256\hbar^5} \approx 4 \times 10^{-7} \text{ m}^2/\text{s}^3. \quad (56)$$

We now interpret the parameter ε_u as the rate of transfer of (specific) kinetic energy v_X^2 in a turnaround time l_X/v_X . That kinetic energy is continuously transferred across haloes to larger and larger scales until the characteristic mass m_h^* , which determines the halo structure and dynamics (Fig. 8). The simulation and observational evidence involving the key parameter ε_u is discussed in Sections 6 to 10.

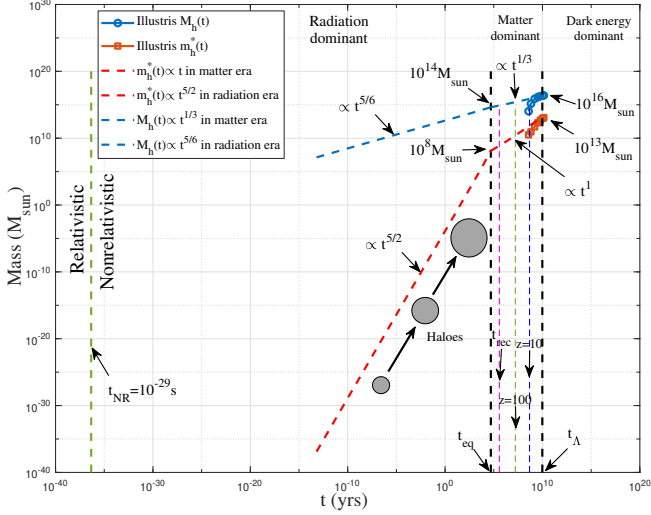


Figure 6. The evolution of the characteristic halo mass $m_h^*(t)$ (red line) and total mass in all haloes $M_h(t)$ (blue line) in the radiation and matter eras to match the blue and red symbols from Illustris simulations (Sections 6 to 10). Evolution in the matter era is also presented in Fig. 7. In the radiation era, $m_h^* \propto t^{5/2}$ and $M_h \propto t^{5/6}$. The average waiting time between two successive merges decreases rapidly over time with $\tau_g^* \propto t^{-3/2}$. In the matter era, $m_h^* \propto t^1$ and $M_h \propto t^{1/3}$, and a constant average waiting time $\tau_g^* \approx 10^{-41} \text{ s} \approx 18\pi^2 t_p$, where $t_p = 5.4 \times 10^{-44} \text{ s}$ is the Planck time. Table 1 summarizes the evolution of structures in both eras. The halo mass m_h^* can reach around $10^8 M_\odot$ at matter-radiation equality.

5 NONLINEAR HALO EVOLUTION IN RADIATION ERA

In the radiation era, density perturbations are suppressed on large scales (linear regime) greater than the characteristic mass m_h^* . On small scales (nonlinear regime) less than m_h^* , haloes can form by direct collision and gravitational collapse (Fig. 4). After the formation of the smallest two-particle haloes at $t_X = 10^{-6} \text{ s}$, the hierarchical structure formation takes over, and the characteristic halo mass m_h^* increases over time (Fig. 5). On small scales in the nonlinear regime, micro-haloes grow by merging with X particles to form larger and larger haloes. In this section, we discuss the evolution of nonlinear structures in the radiation era.

The hierarchical merging of structures is fundamental and complex. In a finite time interval Δt , hierarchical merging could involve multiple substructures merging into a single large structure. However, for an infinitesimal interval $\Delta t \rightarrow 0$, the most frequent merging should involve a single X particle and a halo, an elementary and fundamental step for hierarchical structure formation (two-body collapse [80]). Similarly to the formation of two-particle haloes, halo evolution in the radiation era involves a direct collision with a cross-section $\sigma_d = \pi r_h^2$ that depends on the halo mass $r_h \propto m_h^{1/3}$. We consider the average waiting time τ_g as the time between two successive merges between the halo and the particles. This waiting time is just the direct collision time in the radiation era ($\tau_g \equiv \tau_{dc}$),

$$\tau_g = \tau_{dc} = \frac{4}{3} \left(\frac{r_{DM}}{r_h} \right)^2 \frac{r_{DM}}{V_{||}} \propto m_h^{-\lambda}, \quad (57)$$

where $r_{DM} \propto a$ is the mean separation and $\lambda = 2/3$ is a halo geometry parameter because of $r_h \propto m_h^{1/3}$. After every merge with a single particle, the halo mass increases by the particle mass m_X .

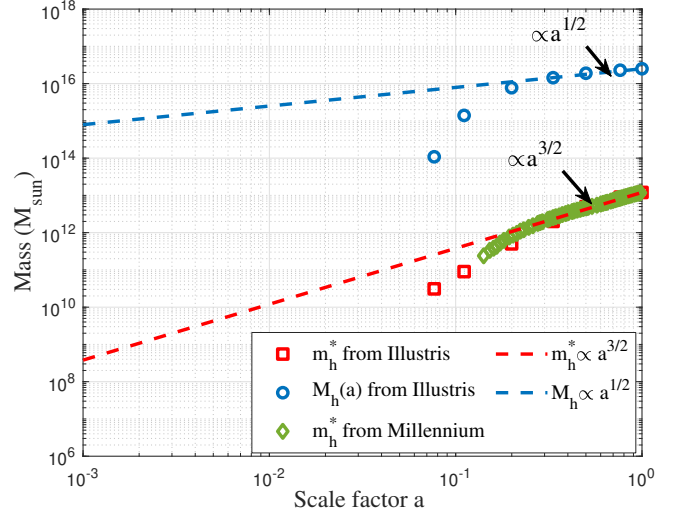


Figure 7. The evolution of the characteristic halo mass $m_h^*(t)$ (red dashed) and total halo mass M_h (blue dashed) in the matter era, where $m_h^* \propto a^{3/2} \propto t$ and $M_h \propto a^{1/2} \propto t^{1/3}$. Results from different cosmological N-body simulations (symbols) are also presented that are in agreement with the prediction of Eq. (61). The deviation at high redshift can be due to the limited mass resolution in N-body simulations.

Therefore, the evolution of the halo mass m_h and m_h^* now reads

$$\frac{dm_h}{dt} = \frac{m_X}{\tau_g} \quad \text{and} \quad \frac{dm_h^*}{dt} = \frac{m_X}{\tau_g^*}. \quad (58)$$

Since haloes should have a constant density ratio to the background density ($32\pi^2$ from the spherical collapse model), we have

$$\rho_h = \frac{m_h}{\frac{4}{3}\pi r_h^3} = 32\pi^2 \rho_{rad} \propto a^{-4}. \quad (59)$$

Solving these equations leads to the scaling

$$\tau_g \propto m_h^{-2/3} a^{1/3} \quad \text{and} \quad r_h \propto m_h^{1/3} a^{4/3}. \quad (60)$$

For haloes with the characteristic mass m_h^* and size r_h^* , we have the scaling $r_h^* \propto a^3 \propto t^{3/2}$, $m_h^* \propto a^5 \propto t^{5/2}$ using Eqs. (58) and (60). The average waiting time for haloes of mass m_h^* follows $\tau_g^* \propto a^{-3} \propto t^{-3/2}$. The waiting time due to direct collision rapidly decreases due to the fast growth of the halo size r_h^* and the rapid increase in the cross-section. In addition, the total mass $M_h(t)$ of dark matter contained in all haloes also increases with time. With the geometry parameter $\lambda = 2/3$, the total halo mass is $M_h \propto m_h^{*1-\lambda}$ [87] such that $M_h \propto a^{5/3} \propto t^{5/6}$.

For comparison, structure evolution in the matter era is dominated by gravity. The waiting time τ_g is inversely proportional to the halo potential $\tau_g \propto (Gm_h/r_h)^{-1}$ [87, 79]. To understand this, we consider a particle to merge with a halo of mass m_h and size r_h . The local velocity dispersion σ^2 of that particle (or the local temperature T) depends on the local gravitational potential, i.e., $T \propto \sigma^2 \propto Gm_h/r_h$. The probability P for a successful merge is $P \propto e^{-1/T}$. Therefore, the waiting time $\tau_g \propto 1 - P \propto 1/T$ for high temperature T . A larger halo with higher potential means higher temperature and shorter waiting time $\tau_g \propto T^{-1}$. Larger haloes accrete mass more quickly with a shorter waiting time, where $\tau_g \propto m_h^{-2/3}$ with $r_h \propto m_h^{1/3}$ [87, 79]. Haloes of characteristic mass m_h^* have the shortest waiting time τ_g^* .

Therefore, corresponding equations in the matter era are

$$\begin{aligned} \frac{dm_h}{dt} &= \frac{t_0}{10^{13}M_\odot} = \frac{m_X}{\tau_g}, \\ \tau_g &\propto (Gm_h/r_h)^{-1}, \\ \rho_h &= \frac{m_h}{\frac{4}{3}\pi r_h^3} = 18\pi^2\rho_{DM} \propto a^{-3}. \end{aligned} \quad (61)$$

Solving these equations leads to the scalings in the matter era:

$$\tau_g \propto m_h^{-2/3}a \quad \text{and} \quad r_h \propto m_h^{1/3}a. \quad (62)$$

For haloes with the characteristic mass m_h^* and size r_h^* , we have the scaling $r_h^* \propto t$, $m_h^* \propto t$, and the constant waiting time $\tau_g^* \propto t^0$ in the matter era. The total mass in all haloes $M_h \propto m_h^{*1/3} \propto t^{1/3}$.

Table 1 summarizes the evolution of mass and energy in both the radiation and matter eras. Figure 6 presents the evolution of the characteristic halo mass m_h^* and the total halo mass M_h in both eras, while Fig. 7 presents the particular evolution in the matter era. Different cosmological N-body simulations confirm the evolution of the halo mass as predicted by Eq. (61). The characteristic halo mass $m_h^* \propto t$ and the total halo mass $M_h^* \propto t^{1/3}$ in the matter era. With $m_h^*(z=0) \approx 10^{13}M_\odot$ and $M_h(z=0) \approx 10^{16}M_\odot$ from Illustris simulation, the evolution of m_h^* and M_h can be fully determined for the radiation (left equations) and matter (right equations) eras as

$$\begin{aligned} m_h^* &= m_h^*(t_{eq}) \left(\frac{t}{t_{eq}}\right)^{5/2} \quad \text{and} \quad m_h^* = m_h^*(t_{eq}) \left(\frac{t}{t_{eq}}\right), \\ M_h &= M_h(t_{eq}) \left(\frac{t}{t_{eq}}\right)^{5/6} \quad \text{and} \quad M_h = M_h(t_{eq}) \left(\frac{t}{t_{eq}}\right)^{1/3}, \end{aligned} \quad (63)$$

where the characteristic halo mass and total halo mass at matter-radiation equality are $m_h^*(t_{eq}) = 5 \times 10^7 M_\odot$ and $M_h(t_{eq}) = 4.3 \times 10^{14} M_\odot$, respectively, where $t_{eq} = 50000$ yrs.

Using Eq. (58), the waiting time τ_g^* for characteristic haloes is:

$$\begin{aligned} \tau_g^* &= \tau_g^*(t_{eq}) (t/t_{eq})^{-3/2}, \quad (\text{radiation era}), \\ \tau_g^* &= \tau_g^*(t_{eq}) = \frac{m_X t_{eq}}{m_h^*(t_{eq})}, \quad (\text{matter era}). \end{aligned} \quad (64)$$

The average waiting time decreases rapidly in the radiation era ($\tau_g \propto t^{-3/2}$) and reaches a constant value in the matter era due to characteristic mass $m_h^* \propto t$ (Eq. (61)). That constant value is dependent on the particle mass m_X ,

$$\tau_g^*(t > t_{eq}) = \frac{m_X}{m_h^*(t)} t = \frac{m_X}{m_h^*(t=t_0)} t_0. \quad (65)$$

With present characteristic halo mass of $10^{13}M_\odot$ and t_0 of the age of the universe, for particles of critical mass $m_X = m_{Xc} = 10^{12}$ GeV, the waiting time is (from Eq. (65))

$$\tau_g^* \approx 10^{-41} s \approx 18\pi^2 t_p, \quad (66)$$

where $t_p = 5.4 \times 10^{-44}$ s is the Planck time. Here, $\xi = 18\pi^2$ is the critical density ratio in the matter era. For fixed mass density of dark matter haloes, a higher density ratio ξ means a lower background matter density and, of course, a longer waiting time for X particles to merge with haloes. Therefore, τ_g^* is expected to be proportional to the density ratio ξ [79]. Since the Planck time is the smallest unit of time for any physical processes, particles with a critical mass m_{Xc} have the shortest possible waiting time $18\pi^2 t_p$ [79]. This is another feature of the critical particle mass $m_{Xc} = 10^{12} GeV$.

Table 1. Structure evolution in the radiation era and matter era

Quantity	Symbol	Radiation era	Matter era
Time	t	$\propto a^2$	$\propto a^{3/2}$
Hubble parameter	Ht	1/2	2/3
Large-scale overdensity	δ	a^0	a^1
Large-scale KE	K_{ph}	$\propto a^0$	$\propto a^1$
Small-scale KE	K_{pv}	$\propto t$	$\propto t$
Total mass in all haloes	M_h	$t^{5/6}$	$t^{1/3}$
Characteristic halo mass	m_h^*	$t^{5/2}$	t
Characteristic halo size	r_h^*	$t^{3/2}$	t
Halo waiting time	τ_g	$\propto m_h^{-2/3} a^{1/3}$	$\propto m_h^{-2/3} a^1$

Since Eq. (65) is independent of the dark matter particle model, for matter era, we write the waiting time for any particle mass m_X

$$\frac{\tau_g^*}{18\pi^2 t_p} = \frac{m_X}{m_{Xc}} \quad \text{and} \quad \tau_g^* \propto m_X, \quad (67)$$

where the waiting time in the matter era is proportional to the particle mass. For particles with a mass $m_X \ll m_{Xc}$, the waiting time τ_g^* can be much shorter than the Planck time, which seems unfavorable. Or equivalently, there is not enough time for particles with mass $m_X \ll m_{Xc}$ to form haloes of $10^{13}M_\odot$ as observed in the current epoch unless different mechanisms exist to accelerate the mass accretion in the matter era for particles with a mass smaller than m_{Xc} . However, any faster super-linear halo mass evolution ($m_h^*(t) \propto t^\alpha$ with $\alpha > 1$) will contradict the results of the N-body simulations in Fig. 7.

Due to rapid growth in the radiation era, the characteristic halo mass m_h^* can reach around $10^8 M_\odot$ at the matter-radiation equality. This suggests that the dark matter haloes can reach an immense size earlier than we expected, which might be helpful to explain the JWST's recent discovery of big and bright galaxies as early as $z = 15$ [12]. Table 1 summarizes the evolution of halo structures in both eras. The evolution of kinetic energy on large-scale and small-scale is discussed in Section 9 and presented in Fig. 12.

Up to this point, we have discussed the formation and evolution of nonlinear halo structures in the radiation era (Sections 2 to 5). We identified a critical mass scale m_{Xc} on the order of 10^{12} GeV. Dark matter particles seem to prefer to have a mass of that critical mass because i) particles of this mass lead to the smallest possible structure (Fig. 2); ii) particles of this mass have a direct collision time scale τ_{dc} comparable to the formation time t_X to allow the formation of the smallest and earliest two-particle haloes (Eq. (54)); and iii) particles of this mass have the shortest possible waiting time τ_g^* to allow the formation of haloes observed today as large as $10^{13}M_\odot$ (Eq. (67)). In particular, the last point is that particles of this mass give rise to the appropriate key parameter ε_μ (Eq. (56)) that influence the halo dynamics and density profiles that can be observed. In the following, we will focus on this point with N-body simulations and observational evidence.

6 MASS AND ENERGY CASCADE IN DARK MATTER

While the spherical collapse model is a powerful tool for nonlinear structure evolution on small scales (Section 3), it models the evolution of overdensity on a single fixed mass scale. It neglects the interactions between different scales (or haloes of different masses). In this section, we introduce a new type of analytical tool that focuses on the mass and energy flow across various scales, i.e., the mass and energy cascade in dark matter flow [79]. This provides a "top-down"

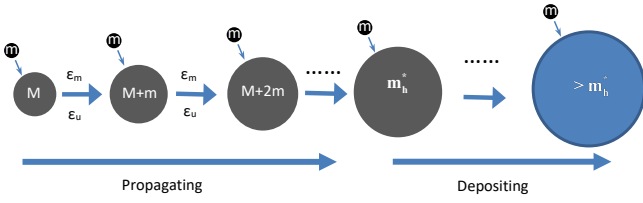


Figure 8. Schematic plot for the inverse mass and energy cascade for hierarchical structure formation of dark matter haloes. Individual haloes accrete mass irregularly on short time scales with discrete jumps through minor and major mergers. However, by averaging over time and the halo ensemble, the equivalent description can be: haloes of mass M merging with a single merger (free DM particles of mass m) leads to a mass and energy flux to a larger scale $M + m$, that is, the halo of mass M moving into the next mass scale $M + m$ after merging. Because haloes have finite mass and kinetic energy, this facilitates a continuous mass and energy cascade from small to large scales across haloes of different masses. Scale-independent mass and energy flux (ε_m and ε_u are independent of mass scale M) are expected in the propagation range ($M < m_h^*$). The potential energy is directly cascaded from large to small scales at a rate of $-7/5 \varepsilon_u$ (see Eq. (88)). The cascade rate becomes scale-dependent in the deposition range ($M > m_h^*$). This concept is quantitatively demonstrated by Illustris simulations in Figs. 10 and 15.

approach to postulate dark matter properties from the large-scale behavior of dark matter haloes. We will first introduce the concepts of mass and energy cascade, which can be directly demonstrated and confirmed by N-body simulation results in Sections 7, 8, and 9.

First, long-range gravity requires the formation of a broad spectrum of haloes to maximize the entropy of the self-gravitating collisionless system [89]. We note that highly localized haloes are a major manifestation of non-linear gravitational collapse [55, 16]. As the building blocks of dark matter flow (counterpart to the "eddies" in turbulence), haloes facilitate an inverse mass cascade from small to large mass scales that are absent in turbulence. The "inverse" stands for the direction of cascade from small to large scales, in contrast to the "direct" cascade from large to small scales. The halo-mediated inverse mass cascade is fully consistent with hierarchical structure formation, where haloes grow by a series of sequential merging. In a more realistic picture, individual haloes accrete mass irregularly on short-time scales with discrete jumps through minor and major mergers. However, if we focus on the averaged mass accretion for an ensemble of haloes of the same mass, the averaged halo growth can be much smoother on a larger time scale. On average, this can be equivalently described by continuous merging with minor mergers.

The averaged formation of the halo structure is shown in Fig. 8. Haloes pass their mass onto larger and larger haloes until the growth of the halo mass becomes dominant over the propagation of the mass through haloes of different scales. Consequently, there is a continuous cascade of mass from the smaller to the larger mass scales with mass flux ε_m independent of the mass scale in a certain range of scales (the propagation range). In that range, the mass flux into any mass scale balances the mass flux out of the same scale so that the total mass of haloes at that scale does not vary with time; i.e., these haloes propagate mass to large scales (small-scale permanence in Fig. 11). The mass cascaded from small scales is finally consumed to grow haloes in the deposition range at scales with $M > m_h^*$. From this description, the mass cascade can be described as follows.

"Little haloes have big haloes, That feed on their mass;
And big haloes have greater haloes, And so on to growth."

Second, haloes have finite kinetic and potential energy. Therefore, accompanied by the mass cascade, there exists also a simultaneous energy flux (energy cascade at a rate of ε_u) across haloes on different

scales. The kinetic energy is also cascaded from small to large scales (the same as the mass cascade), whereas the potential energy is cascaded in the opposite direction. This happens because the potential energy is defined to be negative, while the kinetic energy is positive. When dark matter flow reaches a statistically steady state, the rate of mass and energy cascade must be scale independent (i.e., ε_m and ε_u in Fig. 8 are independent of mass scale M). If this is not the case, there would be a net accumulation of mass and energy on some intermediate-mass scale below m_h^* . We exclude this possibility and require that the statistical structures of haloes be self-similar and scale-free for haloes smaller than m_h^* . This leads to a scale-independent cascade up to a critical mass m_h^* . The entire concept can be demonstrated by Illustris simulations in Section 7 (see Figs. 10 and 15). The value of $\varepsilon_u \approx 10^{-7} m^2/s^3$ for the energy cascade is estimated in Eq. (89). The scaling laws associated with the energy cascade will be derived in Section 11.

Finally, the mass and energy cascades are only relevant on small scales in the nonlinear regime, where haloes of different sizes are the dominant structures ($r_{fs} < r < r_t$ in Fig. 1). The structure evolution on small scales is highly nonlinear. It can only be studied by N-body simulations with the Newtonian approximation and simplified analytical tools (spherical collapse model, etc., in Section 3). The mass and energy cascade in this section provides another useful approach to understanding the nonlinear structure evolution.

7 INVERSE MASS CASCADE IN HALO MASS SPACE

In this section, we present a quantitative description of the mass cascade. To validate the concepts, we used results from the large-scale cosmological Illustris simulation (Illustris-1-Dark) [54]. Illustris is a suite of large-volume cosmological dark matter only and hydrodynamical simulations. The selected Illustris-1-Dark is a dark matter only simulation of a 106.5Mpc^3 cosmological volume with 1820^3 DM particles for the highest resolution. Each DM particle has a mass around $m_p = 7.6 \times 10^6 M_\odot$. The gravitational softening length is around 1.4 kpc. The simulation has cosmological parameters of dark matter density $\Omega_{DM} = 0.2726$, dark energy density $\Omega_{DE} = 0.7274$ at $z = 0$, and Hubble constant $h = 0.704$. The haloes in the simulation were identified using a standard Friends of Friends (FoF) algorithm with a link length parameter $b = 0.2$. Then, all dark matter particles were divided into halo particles with a total mass M_h and out-of-halo particles that do not belong to any halo. Therefore, M_h is the total mass of all haloes. We will focus on the evolution of mass and energy in haloes of different mass m_h .

First, we can mathematically express the mass flux (Π_m) across haloes of different sizes as

$$\begin{aligned} \Pi_m(m_h, a) &= - \int_{m_h}^{\infty} \frac{\partial}{\partial t} [M_h(a) f_M(m, m_h^*)] dm, \\ &= - \frac{\partial}{\partial t} \left[\int_{m_h}^{\infty} M_h(a) f_M(m, m_h^*) dm \right] = - \frac{\partial \Lambda_m}{\partial t}, \end{aligned} \quad (68)$$

where a is the scale factor and M_h is the total mass in all haloes of all sizes. Here $f_M(m_h, m_h^*)$ is the halo mass function, that is, the probability distribution of the total mass M_h in all haloes of different mass m_h . The total mass of all haloes with a mass between m_h and $m_h + dm$ should be $M_h f_M(m_h, m_h^*) dm$. The cumulative mass function $\Lambda_m(m_h, a)$ represents the total mass in all haloes greater than the scale m_h , that is,

$$\Lambda_m(m_h, a) = \int_{m_h}^{\infty} M_h(a) f_M(m, m_h^*) dm. \quad (69)$$

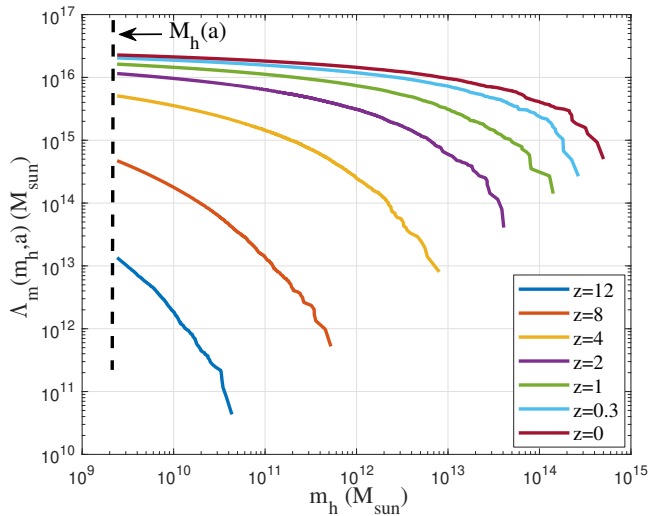


Figure 9. The variation of cumulative mass function $\Lambda_m(m_h, a)$ with halo mass scale m_h at different redshifts z from Illustris-1-Dark simulation. The total mass $M_h(a)$ in all haloes of all sizes is computed with $m_h \rightarrow 0$, i.e. $M_h(a) = \Lambda_m(m_h = 0, a)$. Using function $\Lambda(m_h, a)$, the rate of mass cascade $\Pi_m(m_h, a)$ in Eq. (68) was computed and presented in Fig. 10.

Figure 9 plots the variation of the cumulative mass function $\Lambda_m(m_h, a)$ with mass scale m_h and redshifts z from the Illustris-1-Dark simulation. The total halo mass can be obtained by setting $m_h \rightarrow 0$ in Eq. (69), i.e. $M_h(a) = \Lambda_m(m_h \rightarrow 0, a)$.

The time derivative of Λ_m describes the mass flux from all haloes below the scale m_h to all haloes above the scale m_h , i.e., the rate of mass cascade Π_m in Eq. (68). In N-body simulations, we use the difference of Λ_m at two different redshifts z_1 (or t_1) and z_2 (or t_2) to compute the time derivative and obtain the mass cascade rate Π_m . For Illustris cosmology, the time t at redshift z is computed from

$$a(t) = \frac{1}{1+z(t)} = \left(\frac{\Omega_m}{\Omega_\Lambda}\right)^{1/3} \sinh^{2/3} \left(\frac{t}{2/(3H_0\sqrt{\Omega_\Lambda})} \right). \quad (70)$$

Figure 10 presents the variation of the rate of the mass cascade $\Pi_m(m_h, a)$ with the mass scale m_h using the values of the cumulative mass function Λ_m at two different redshifts z_1 and z_2 in Fig. 9. In the schematic diagram in Fig. 8, we propose the concept that the rate of cascade $\Pi_m(m_h, a)$ is independent of the scale m_h for $m_h < m_h^*$ in the propagation range since we require that the statistical structures of the haloes be self-similar and scale-free for haloes smaller than m_h^* . The simulation results confirm this concept, that is, the existence of a propagation range with a scale-independent cascade rate $\varepsilon_m(a) \equiv \Pi_m(m_h, a)$ for scales m_h below a critical mass scale m_h^* . After reaching a statistically steady state, that scale-independent rate $\varepsilon_m(a) \propto a^{-1}$, that is, decreases with time and is about $-0.02M_\odot/s$ at $z = 0$ from the Illustris simulation. The time dependence of $\varepsilon_m(a) \propto a^{-1}$ due to background expansion means a decreasing mass flux in the halo mass space.

As described in the schematic plot in Fig. 8, all masses cascaded from the smallest scale are propagated through the propagation range and are consumed mainly to grow haloes greater than m_h^* in the deposition range. To explain this, we write the scale-independent ε_m in the propagation range as

$$\varepsilon_m(a) \equiv \Pi_m(m_h, a) = -\frac{\partial M_h}{\partial t} \propto a^{-1} \quad \text{for } m_h < m_h^*, \quad (71)$$

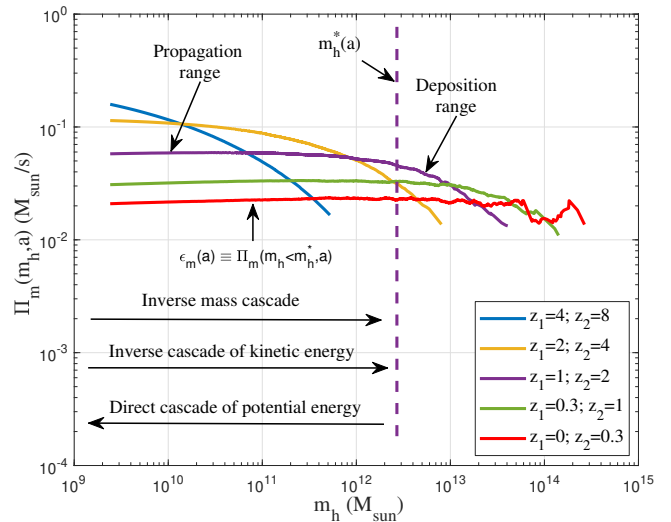


Figure 10. Variation of the rate of inverse mass cascade $\Pi_m(m_h, a)$ (Eq. (68), < 0 for 'inverse'), calculated by the values of the cumulative mass function Λ_m (Eq. (69)) at two different redshifts z_1 and z_2 from Fig. 9. After reaching a statistically steady state, the simulation confirms the existence of a propagation range for the scales $m_h < m_h^*(a)$, a characteristic mass scale that increases with time. A scale-independent rate of the mass cascade $\varepsilon_m(a) \equiv \Pi_m(m_h, a)$ can be identified in the propagation range, which decreases with time ($\varepsilon_m(a) \propto a^{-1}$) and is around $-0.02M_\odot/s$ at $z = 0$. Haloes in the propagation range pass their mass to larger haloes, where the group mass m_g (total mass of all haloes with the same mass m_h) reaches a steady state (see Eq. (72) and Fig. 11). There also exists a simultaneous energy cascade discussed in Section 8.

which further requires (from Eq. (68))

$$\frac{\partial \Pi_m}{\partial m_h} = \frac{\partial \varepsilon_m}{\partial m_h} = \frac{\partial}{\partial t} [M_h(a) f_M(m_h, m_h^*)] = \frac{1}{m_p} \frac{\partial m_g}{\partial t} = 0. \quad (72)$$

From this, we found that the total mass m_g for a group of haloes with the same mass m_h reaches a steady state and does not vary over time for $m_h < m_h^*$. Here, the halo group mass m_g is written as

$$m_g(m_h) = M_h(a) f_M(m_h, m_h^*) m_p = N_h m_h, \quad (73)$$

where m_p is the mass resolution, and N_h is the number of haloes in that group. Due to the steady-state group mass m_g , these haloes propagate the mass from small scales to grow haloes greater than m_h^* , that is, the "propagation range." This concept can be clearly demonstrated by the Illustris simulations in Fig. 11 such that the halo number density follows $N_h \propto m_h^{-\lambda-1}$ in that range and is actually independent of the redshift. The mass of the halo group, m_g of different redshifts, collapses onto the same time-independent power law $m_g \propto m_h^{-\lambda}$ ($\lambda = 0.88$ from the Illustris simulation). This is the "so-called" small-scale permanence for the halo group mass (m_g) due to the scale-independent mass cascade in Fig. 10, i.e., the mass flux into low-mass halo group balances the mass flux out of the same group. This is also in agreement with the slow decline of the number density of low-mass haloes at low redshift [49]. The small-scale permanence also exists for halo density profiles due to the scale-independent energy cascade (Fig. 24). The halo mass function and density profile can also be analytically derived based on the mass and energy cascade [87].

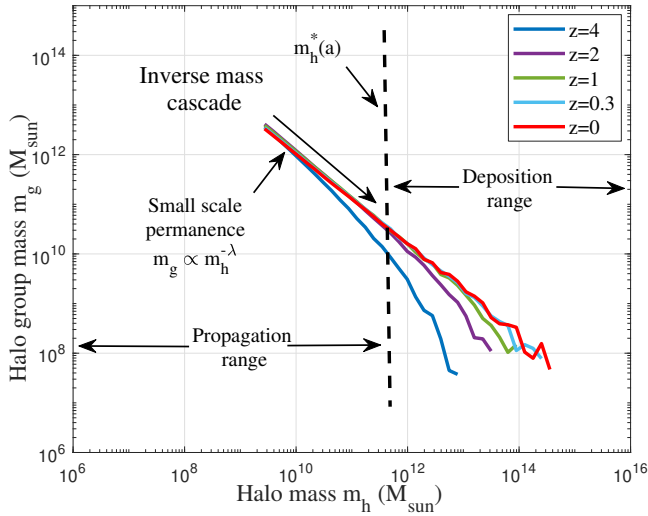


Figure 11. The variation of halo group mass $m_g(m_h)$ for all haloes of the same mass m_h at different redshifts z from Illustris-1-Dark simulation. The figure demonstrates the small-scale permanence of the group mass m_g . Once the statistically steady state is established ($z \leq 4$), the rate of the inverse mass cascade ε_m becomes scale independent (Eq. (72)) such that the mass of the halo group m_g at different redshifts z collapses into a time-independent power law $m_g \propto m_h^{-\lambda}$ on small mass scales with the halo geometry parameter $\lambda \approx 0.88$ [87]. This is the so-called "propagation range," where the mass cascaded from the smallest (DM particle) scale is propagated to larger scales, that is, a constant group mass m_g . The cascaded mass is eventually consumed to grow haloes greater than m_h^* (the "deposition range"). The propagation range gradually extends to large scales ($m_h^*(a)$ increases over time) due to the continuous inverse mass cascade.

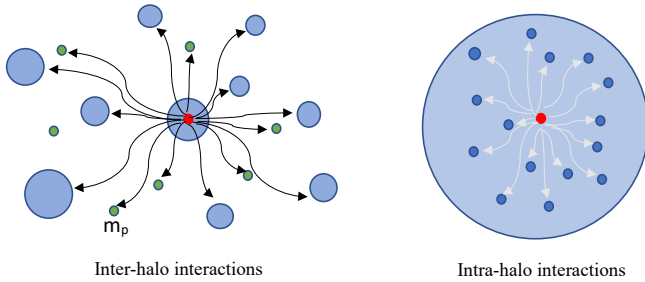


Figure 12. Decomposition of kinetic energy into the contributions due to inter-halo interactions on a longer distance and intra-halo interactions on a shorter distance. The inter-halo interactions with all other particles in different haloes and all out-of-halo particles (green) are weaker on larger scales and in the linear regime (K_{ph}). The intra-halo interactions with all other particles in the same halo are stronger, on smaller scales, and in the nonlinear regime (K_{pv}). The evolution of two KEs is also presented in Fig. 5 and Table 1.

8 ENERGY CASCADE IN HALO MASS SPACE

Since haloes have finite energy, there is also a simultaneous energy cascade associated with the mass cascade (Fig. 10). This section presents a quantitative description of the energy cascade in the halo mass space.

To better describe the energy cascade, we start by decomposing the particle kinetic energy into two parts of different nature. In N -body simulations, every halo particle, characterized by a mass m_p , and a velocity vector \mathbf{v}_p , should belong to one and only one parent halo. The particle velocity \mathbf{v}_p can be decomposed as [89]

$$\mathbf{v}_p = \mathbf{v}_h + \mathbf{v}'_p, \quad (74)$$

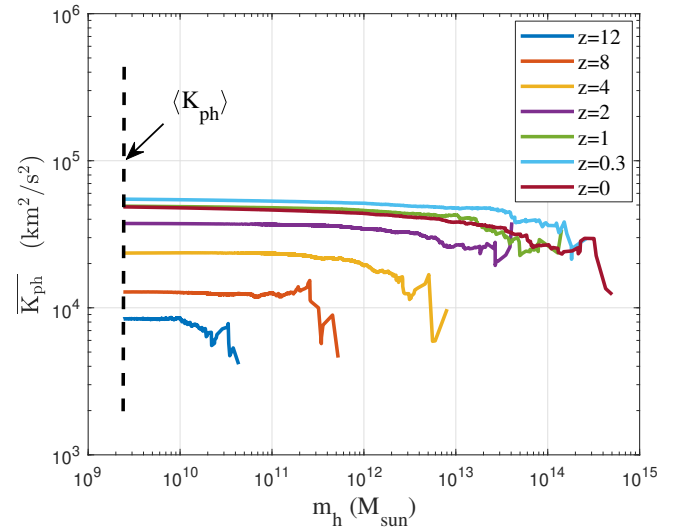


Figure 13. The variation of mean halo kinetic energy $\overline{K_{ph}}$ with halo mass scale m_h at different redshifts z from Illustris-1-Dark simulation. The mean halo kinetic energy in all haloes of all sizes is denoted as the black dashed line with $m_h \rightarrow 0$, i.e. $\langle K_{ph} \rangle = \overline{K_{ph}}(m_h \rightarrow 0, a)$. This figure will be used to compute the evolution of mean halo kinetic energy $\langle K_{ph} \rangle$ for all halo particles in Fig. 18. Due to the long-range interaction with particles from different haloes, halo kinetic energy increases with time in early matter dominant universe (i.e., the linear regime with $\langle K_{ph} \rangle \propto t^{2/3}$ shown in Fig. 18). It slightly decreases at low redshift in the dark energy dominant universe due to the accelerated expansion.

namely, the halo mean velocity, $\mathbf{v}_h = \langle \mathbf{v}_p \rangle_h$, and the velocity fluctuation, \mathbf{v}'_p . Here, $\langle \rangle_h$ represents the average of all particles in the same halo, and \mathbf{v}_h represents the velocity of that halo.

Consequently, the total kinetic energy K_p of a given halo particle can be divided into $K_p = K_{ph} + K_{pv}$. As shown in Fig. 12, here $K_{ph} = \mathbf{v}_h^2/2$ (halo kinetic energy) is the contribution from the motion of entire haloes \mathbf{v}_h due to the inter-halo interaction of that particle with all other particles in different haloes and all out-of-halo particles (green). This part of the kinetic energy is related to interactions on large scales in the linear regime. While $K_{pv} = \mathbf{v}'_p{}^2/2$ (virial kinetic energy) is the contribution of the velocity fluctuation \mathbf{v}'_p due to the intra-halo interaction of that particle with all other particles in the same halo. This part of the kinetic energy is from halo virialization and is due to interactions on a shorter distance and smaller scales in the non-linear regime. Like the energy cascade associated with nonlinear interactions in turbulence, the energy cascade in this work is focused on the cascade of the virial kinetic energy K_{pv} across different scales in the deeply non-linear regime.

Similar to the cumulative mass function Λ_m in Eq. (69), the cumulative kinetic energies (Λ_{ph} and Λ_{pv}) represent the total kinetic energies K_{ph} and K_{pv} in all haloes greater than m_h , such that

$$\begin{aligned} \Lambda_{ph}(m_h, a) &= \int_{m_h}^{\infty} M_h(a) f_M(m, m_h^*) K_{ph} dm, \\ \Lambda_{pv}(m_h, a) &= \int_{m_h}^{\infty} M_h(a) f_M(m, m_h^*) K_{pv} dm, \end{aligned} \quad (75)$$

$$K_{ph} = \frac{3}{2} \sigma_h^2(m, a) \quad \text{and} \quad K_{pv} = \frac{3}{2} \sigma_v^2(m, a).$$

Here, σ_h^2 and σ_v^2 are the dispersion of the one-dimensional velocity for the halo velocity \mathbf{v}_h and the velocity fluctuation \mathbf{v}'_p [87].

Next, we will use the cumulative kinetic energy and cumulative

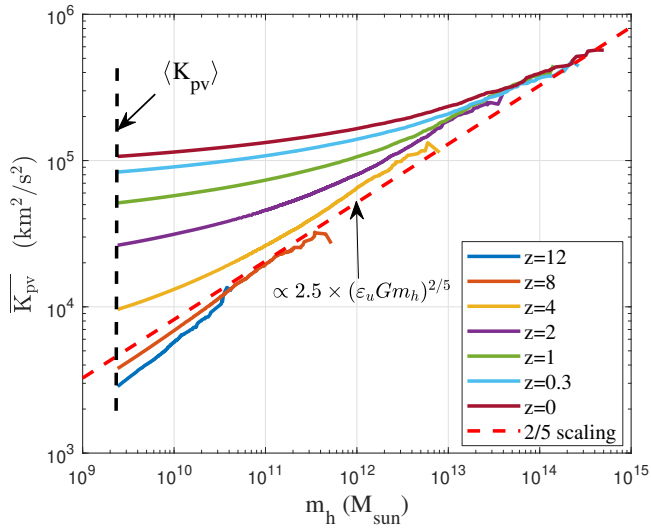


Figure 14. The variation of mean virial kinetic energy $\overline{K_{pv}}$ with halo mass scale m_h at different redshifts z from Illustris-1-Dark simulation. The mean virial kinetic energy in all haloes of all sizes is denoted as the black dashed line with $m_h \rightarrow 0$, that is, $\langle K_{pv} \rangle = \overline{K_{pv}}(m_h \rightarrow 0, a)$ in Fig. 18. This figure is used to calculate the rate of the energy cascade ϵ_u in Fig. 15. Due to the virialization of the halo and the interaction with particles in the same halo, the virial kinetic energy K_{pv} increases with time (the non-linear regime with $\langle K_{pv} \rangle \propto t^1$ shown in Fig. 18). The dark energy has negligible effects on the virial kinetic energy due to the bounded halo structure. The 2/5 scaling ($\overline{K_{pv}} \propto m_h^{2/5}$ for $m_h \rightarrow \infty$) is also presented for comparison (Eq. (104)).

mass Λ_m to calculate the mean specific halo kinetic energy (energy per unit mass) $\overline{K_{ph}}$ and the virial kinetic energy $\overline{K_{pv}}$ in all haloes above any mass scale m_h , that is,

$$\overline{K_{ph}} = \frac{\Lambda_{ph}}{\Lambda_m} \quad \text{and} \quad \overline{K_{pv}} = \frac{\Lambda_{pv}}{\Lambda_m}. \quad (76)$$

Figures 13 and 14 plot the variation of the (specific) halo kinetic energy $\overline{K_{ph}}$ and the virial kinetic energy $\overline{K_{pv}}$ with the halo mass m_h from Illustris simulations. The halo kinetic energy is relatively independent of m_h . The virial kinetic energy increases with the mass of the halo m_h with $\overline{K_{pv}} \propto m_h^{2/5}$ for larger haloes. This can be explained by the scaling laws in Eq. (104). Both kinetic energies increase with time but with different scaling behavior due to the nature of interactions in the linear and nonlinear regimes (Fig. 18).

Next, we will focus on the energy cascade of the specific virial kinetic energy K_{pv} due to nonlinear interactions on small scales. For the inverse mass cascade in Eq. (68), the change in total halo mass above the scale m_h , that is, the cumulative mass function $\Lambda_m(m_h, a)$, comes entirely from the mass cascade or the interactions between all haloes below the scale m_h and all haloes above m_h . Similarly, the change in the (specific) virial kinetic energy $\overline{K_{pv}}$ for all haloes above the scale m_h comes entirely from the energy cascade due to interactions between haloes below and above the scale m_h . This is because, without an energy cascade, haloes above the scale m_h should be in virial equilibrium, where the specific kinetic energy $\overline{K_{pv}}$ is constant and conserved with time (see Eq. (84) for an explanation), just as the total halo mass above the scale m_h is conserved without a mass cascade. Therefore, similar to the mass cascade Π_m in Eq.

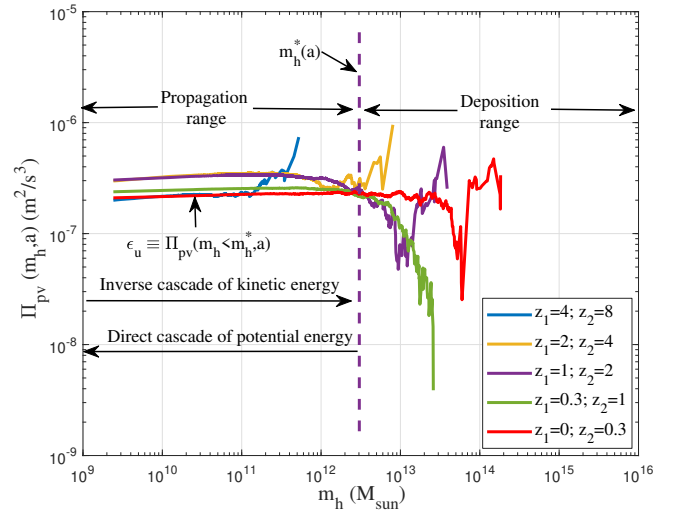


Figure 15. The variation of the rate of energy cascade $\Pi_{pv}(m_h, a)$ (Eq. (77)) with halo mass scale m_h at different redshifts z from Illustris-1-Dark simulation. A scale-independent constant rate of ϵ_u can be identified in the propagation range for an inverse cascade of virial kinetic energy K_{pv} from the smallest scale (single DM particle) to larger scales. That rate is also relatively independent of time and is around $\epsilon_u = -2.5 \times 10^{-7} \text{m}^2/\text{s}^3$ (also see Fig. 18). There also exists a simultaneous direct cascade of potential energy from large to the smallest scale at a rate of $-7/5 \epsilon_u$ (see Eq. (88)).

(68), the rate of cascade for the virial kinetic energy K_{pv} reads

$$\begin{aligned} \Pi_{pv}(m_h, a) &= -\frac{\partial}{\partial t} \left(\overline{K_{pv}} \right) = -\frac{\partial}{\partial t} \left(\frac{\Lambda_{pv}}{\Lambda_m} \right) \\ &= -\frac{\partial}{\partial t} \int_{m_h}^{\infty} \frac{M_h(a) f_M(m, m_h^*) K_{pv}}{\int_{m_h}^{\infty} M_h(a) f_M(m, m_h^*) dm} dm, \end{aligned} \quad (77)$$

where $\overline{K_{pv}}$ is defined in Eq. (76), i.e. the specific virial kinetic energy in all haloes greater than m_h . Similar to Eq. (68), Eq. (77) describes the rate of transfer of specific virial kinetic energy (K_{pv}) from haloes below the scale m_h to haloes above the scale m_h at a rate of Π_{pv} .

Figure 15 plots the variation of Π_{pv} with the halo mass m_h and the redshifts z . The mean (specific) virial kinetic energy $\overline{K_{pv}}$ at two different redshifts z_1 and z_2 in Fig. 14 was used to calculate Π_{pv} in this figure. Similarly to the mass cascade in Fig. 8, if the statistical structures of the haloes are self-similar and scale-free for haloes smaller than the characteristic mass m_h^* , the rate of the energy cascade ϵ_u should also be independent of the scale m_h for $m_h < m_h^*$, i.e. the energy flux into a given group of haloes should balance the energy flux out of the same group. The simulation results confirm a scale- and time-independent rate of cascade ϵ_u . Therefore, in the propagation range ($m_h < m_h^*$),

$$\epsilon_u \equiv \Pi_{pv}(m_h, a) = -\frac{\partial \langle K_{pv} \rangle}{\partial t} \propto \epsilon_m \frac{\langle K_{pv} \rangle}{M_h}, \quad (78)$$

where the rate of energy cascade ϵ_u can be directly related to the rate of mass cascade ϵ_m . Since ϵ_u is scale independent, with continuous injection of virial kinetic energy K_{pv} at a constant rate of ϵ_u on the smallest scale, we should expect the total K_{pv} in all haloes of all sizes to be proportional to time t or $\langle K_{pv} \rangle \propto t$. This is consistent with the solutions of the cosmic energy equation in the next section (Eq. (88) and Fig. 18).

Up to this point, we have discussed the mass and energy cascade in halo mass space. The rate of the energy cascade $\epsilon_u \approx -10^{-7} \text{m}^2/\text{s}^3$

can be estimated for galactic haloes from cosmological simulations (Fig. 15). This is consistent with ε_u obtained on the smallest scale for particles of critical mass m_{X_c} in Eqs. (56). This is, of course, not a mere coincidence as the key parameter ε_u is a constant independent of both scale and time, as shown in Fig. 15. The value of ε_u estimated for small and large haloes should be the same.

9 COSMIC ENERGY EVOLUTION

To better understand the energy cascade, we provide an analysis based on the energy evolution in self-gravitating collisionless dark matter flow. The equations of motion for N collisionless particles in comoving coordinates \mathbf{x} and physical time t read [58]:

$$\frac{d^2 \mathbf{x}_i}{dt^2} + 2H \frac{d\mathbf{x}_i}{dt} = -\frac{Gm_p}{a^3} \sum_{j \neq i}^N \frac{\mathbf{x}_i - \mathbf{x}_j}{|\mathbf{x}_i - \mathbf{x}_j|^3}, \quad (79)$$

where N particles have equal mass m_p . The Hubble parameter $H(t) = \dot{a}/a$. Here, H has a "damping" effect, which leads to the decrease in total energy of the N-body system (Eq. (84) and Fig. 17). In the radiation and matter eras, the Hubble parameter satisfies $Ht = 1/2$ and $Ht = 2/3$, respectively (Table 1). In the dark energy era, the Hubble parameter H approaches a constant value $H_0^* = H_0 \sqrt{\Omega_\Lambda}$, where Ω_Λ is the fraction of dark energy.

Next, we will derive the energy evolution based on equations of motion (Eq. (79)). We first introduce a transformed time variable s as $ds/dt = a^p$, where p is an arbitrary exponent. In terms of the new time variable s , the original Eq. (79) can be transformed to

$$\begin{aligned} \frac{d^2 \mathbf{x}_i}{ds^2} + \frac{d\mathbf{x}_i}{ds} (p+2) a^{-p} H &\equiv a^{-(3+2p)} \frac{\mathbf{F}_i}{m_p}, \\ \frac{\mathbf{F}_i}{m_p} &= -Gm_p \sum_{j \neq i}^N \frac{\mathbf{x}_i - \mathbf{x}_j}{|\mathbf{x}_i - \mathbf{x}_j|^3} = -\frac{\partial P_s}{\partial \mathbf{x}_i}, \end{aligned} \quad (80)$$

where \mathbf{F}_i is the resultant force on particle i from all other particles, while P_s is the total specific potential energy in comoving coordinates. Equation (80) reduces to the original Eq. (79) when $p = 0$. With $p = -2$, the first-order derivative vanishes in Eq. (80) and s is the time variable for integration in N -body simulations. By setting $p = -1$, s is the conformal time. By setting $p = -3/2$ along with $H_0^2 = H^2 a^3$ for the matter era, the equation of motion becomes

$$\frac{d^2 \mathbf{x}_i}{ds^2} + \frac{1}{2} H_0 \frac{d\mathbf{x}_i}{ds} = \frac{\mathbf{F}_i}{m_p}. \quad (81)$$

In this transformed equation for the matter era, the scale factor a is not explicitly involved. The time-dependent Hubble parameter H is replaced by a Hubble constant H_0 (or a constant "damping"), which can offer significant convenience in analytically solving the equations of motion.

We first identify the transformation between velocity \mathbf{v}_i in time variable s and the peculiar velocity \mathbf{u}_i ,

$$\mathbf{v}_i = \frac{d\mathbf{x}_i}{ds} = a^{-p} \frac{d\mathbf{x}_i}{dt} = a^{-p-1} \mathbf{u}_i, \quad \mathbf{u}_i = a \frac{d\mathbf{x}_i}{dt}, \quad (82)$$

$$K_s = K_p a^{-2p-2}, \quad P_s = a P_y,$$

where the kinetic energy K_s and the potential P_s in the transformed equation can now be related to the peculiar kinetic energy K_p and the potential P_y in the physical coordinates.

The energy evolution of the N-body system can be obtained by multiplying $\mathbf{v}_i = d\mathbf{x}_i/ds$ on both sides of Eq. (80) and adding the equation of motion for all particles together [85]. An exact and simple

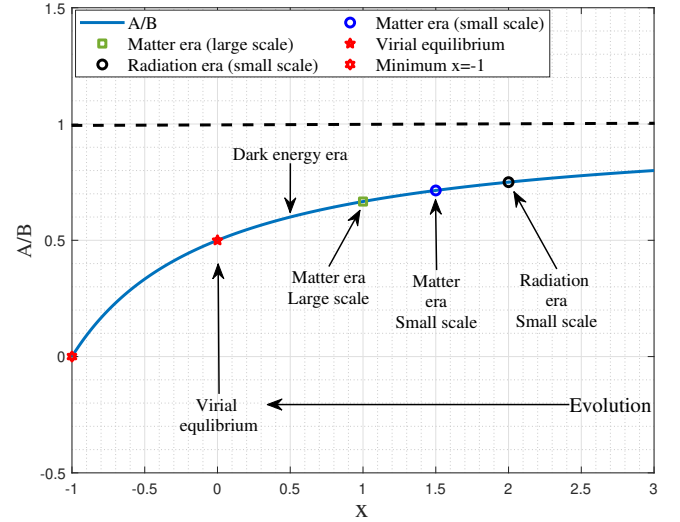


Figure 16. The evolution of A/B for N-body system in different eras. The solid line represents the analytical solution in Eq. (85). Symbols represent the solution for different eras. The initial state $x = \infty$ should have a total energy $E_y = 0$ or $A = B$. In the radiation era, the kinetic energy on small scales evolves as $K_{pv} \propto a^2 \propto t$ such that $A/B = 3/4$ (black circle). In the matter era, the kinetic energy on large scales evolves as $K_{ph} \propto a$ such that $A/B = 2/3$ (green circle), while the kinetic energy on small scales follows $K_{pv} \propto a^{3/2} \propto t$ such that $A/B = 5/7$ (blue circle). For the dark energy era, x decreases to 0 and $A/B \rightarrow 1/2$ so that the system approaches the limiting virial equilibrium (red star). The minimum possible $x = -1$ is also denoted as the limiting state for the dissipative gas in the bulge where the kinetic energy of gases decreases with time as $K_p \propto a^{-1}$ [90].

equation (in time variable s) for the specific kinetic energy K_s and the potential energy P_s can be obtained as

$$\frac{dK_s}{ds} + 2HK_s (p+2) a^{-p} + a^{-(3+2p)} \frac{dP_s}{ds} = 0. \quad (83)$$

By setting $p = 0$ and using the relations in Eq. (82), the exact cosmic energy equation for energy evolution of the N-body system reads

$$\frac{\partial E_y}{\partial t} + H(2K_p + P_y) = 0, \quad (84)$$

which describes the energy evolution in an expanding background. Here K_p is the peculiar kinetic energy, P_y is the potential energy in physical coordinates and $E_y = K_p + P_y$ is the total specific energy. This is also known as the Layzer-Irvine equation [33, 40]. Here, we derive it using a different approach.

Next, we will focus on the solutions of the cosmic energy equation in different eras. Without loss of generality, we can assume that $K_p = Aa^x$ and $P_y = -Ba^x$ and substitute them into Eq. (84), the general solution to the cosmic energy equation reads

$$\frac{A}{B} = \frac{1+x}{2+x}. \quad (85)$$

Solutions at different stages are identified and presented in Fig. 16. First, the case of $x = \infty$ corresponds to an initial state with vanishing total energy $E_y = 0$ or $A = B$. Next, we focus on the evolution in different eras.

(i) For the radiation era, the kinetic energy on large scales (halo kinetic energy K_{ph}) is suppressed and constant over time, similarly to the overdensity δ on large scales (Eq. (44)). However, kinetic energy on small scales increases linearly with time due to the energy cascade across haloes, i.e.,

$$K_{pv} = -\varepsilon_u t \propto a^2 \quad \text{and} \quad K_{ph} = V_{\parallel}^2 / 2 \propto a^0. \quad (86)$$

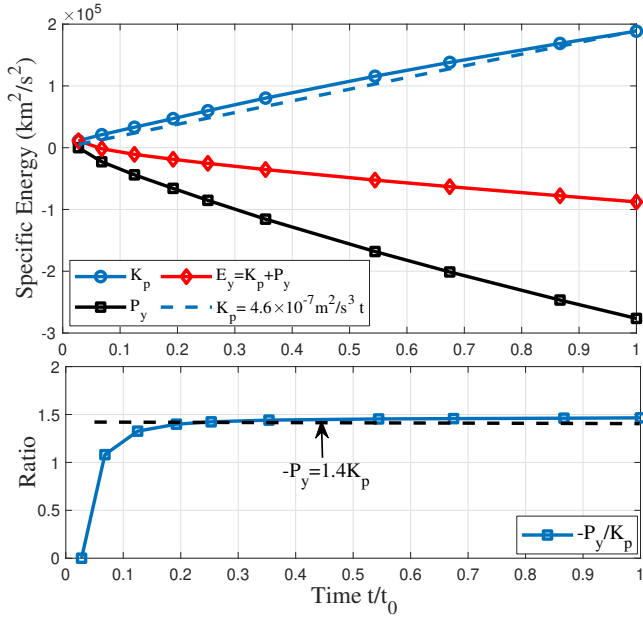


Figure 17. The variation of specific (energy per unit mass) kinetic energy K_p , potential energy P_y , and total energy $E_y = K_p + P_y$ (unit: km^2/s^2) with time t from Virgo SCDM simulation. Solution in Eq. (88) is also presented for comparison with $\varepsilon_u = -4.6 \times 10^{-7} \text{m}^2/\text{s}^3$. Simulation confirms a linear increase of $K_p = -\varepsilon_u t$ with time and negative potential energy $P_y = -1.4K_p$. The total energy $E_y = -0.4K_p$ also decreases with time, which requires a viable mechanism to dissipate the total energy E_y . Similar to the kinetic energy, the Figure reveals a direct cascade of potential energy at a rate of $-1.4\varepsilon_u$ from large to the smallest scale.

The exact solution is, therefore, $A/B = 3/4$ with $x = 2$ from Eq. (85) (the black circle in Fig. 16) for the ratio between kinetic and potential energies on small scales. The evolution of K_{ph} and K_{pv} in the radiation era is also presented in Figs. 5 and 18.

(ii) For the matter era, the kinetic energy on large scales follows $K_{ph} \propto a$ (Eq. (44)), and the exact solution is $A/B = 2/3$ with $x = 1$ (green square in Fig. 16). The kinetic energy on small scales increases linearly with time. The corresponding solution is $A/B = 5/7$ with $x = 3/2$ from Eq. (85) (blue circle in Fig. 16). We have solutions:

$$K_{pv} = -\varepsilon_u t \quad \text{and} \quad K_{ph} = -\varepsilon_u (a/a_\Lambda)^{-1/2} t. \quad (87)$$

Therefore, when most dark matter mass resides in haloes, the kinetic and potential energies of the entire N-body system are dominated by energy on small scales and should be

$$K_p = At = -\varepsilon_u t, \quad P_y = -Bt = \frac{7}{5} \varepsilon_u t. \quad (88)$$

This solution can be directly validated by N-body simulations. Figure 17 was generated from the matter-dominant Virgo simulation (SCDM) with a matter density $\Omega_{DM} = 1$ and dark energy $\Omega_{DE} = 0$. A comprehensive description of this simulation can be found in [25, 34]. The kinetic energy K_p and the potential energy P_y were calculated as the mean energy of all dark matter particles in the N-body system. Figure 17 confirms the solution in Eq. (88), i.e. a linear increase of K_p with time and a negative potential energy $P_y = -1.4K_p$. The total cosmic energy $E_y = -0.4K_p$ also decreases with time, as if "dissipated", even though there is no viscous force in the collisionless dark matter. This energy "dissipation" is balanced by a steady energy cascade from large to small scales when a statistically steady state is established for collisionless dark matter

flow [79]. Therefore, the rate of energy cascade ($\varepsilon_u < 0$ for "inverse") equals the rate of energy "dissipation" and reads

$$\varepsilon_u = -\frac{K_p}{t} = -\frac{3}{2} \frac{u^2}{t} = -\frac{3}{2} \frac{u_0^2}{t_0} \approx -4.6 \times 10^{-7} \frac{\text{m}^2}{\text{s}^3}, \quad (89)$$

where $u_0 \equiv u(t = t_0) \approx 350 \text{km/s}$ is the one-dimensional velocity dispersion of all dark matter particles, and $t_0 \approx 13.7$ billion years is the physical time at present epoch or the age of the universe. Different simulations may have slightly different values of u_0 due to different cosmological parameters. However, the rate of cascade $\varepsilon_u \sim -10^{-7} \text{m}^2/\text{s}^3$ should be a good estimate. This value is also consistent with Eq. (15) for particles with a critical mass of $m_{Xc} = 10^{12} \text{GeV}$.

(iii) For dark energy era, A/B monotonically decreases with x and approaches the limiting virial equilibrium with $A/B = 1/2$ (red star in Fig. 16). In the matter era, the total halo mass M_h and the characteristic halo mass m_h^* increase rapidly over time (Table 2). In the dark energy era, this increase slows down due to the accelerated expansion. Their evolution can be written as (Eqs. (71) and (61))

$$\frac{dM_h}{dt} = -\varepsilon_m \propto a^{-1} \quad \text{and} \quad \frac{dm_h^*}{dt} = \frac{mX}{\tau_g} \propto m_h^{*2/3} a^{-1}. \quad (90)$$

The solutions for halo mass evolution in the dark energy era are

$$M_h(t) = M_h(t_\Lambda) \frac{1 - C_1 \exp(-H_0^* t)}{1 - C_1 \exp(-H_0^* t_\Lambda)}, \quad (91)$$

$$m_h^*(t) = m_h^*(t_\Lambda) \left(\frac{1 - C_2 \exp(-H_0^* t)}{1 - C_2 \exp(-H_0^* t_\Lambda)} \right)^3,$$

where C_1 and C_2 are two constants that can be obtained from boundary conditions at t_Λ . Here, t_Λ and a_Λ are the time and scale factor at the equality of matter and dark energy,

$$a_\Lambda = \left(\frac{\Omega_m}{\Omega_\Lambda} \right)^{1/3}, \quad t_\Lambda = \frac{2 \text{asinh}(1)}{3H_0 \sqrt{\Omega_\Lambda}}, \quad \text{and} \quad H_0^* = H_0 \sqrt{\Omega_\Lambda}. \quad (92)$$

The virial kinetic energy on small scales increases linearly with time in both the radiation and matter eras, i.e. $K_{pv} = -\varepsilon_u t$ (see Table 2 for relevant quantities). In the dark energy era, the rate of the energy cascade ε_u slows down. Kinetic energies on both large and small scales level off as a result of the accelerated expansion. The evolution of kinetic energy follows (from Eq. (78)):

$$\frac{dK_{pv}}{dt} = -\varepsilon_u \propto -\frac{\varepsilon_m}{M_h} K_{pv} \propto a^{-1} \quad \text{and} \quad \frac{dK_{ph}}{dt} \propto a^{-1}, \quad (93)$$

with corresponding solutions (dotted lines in Fig. 18):

$$K_{pv} = -\varepsilon_u t_\Lambda - \varepsilon_u a_\Lambda \int_{t_\Lambda}^t a^{-1} dt, \quad (94)$$

$$K_{ph} = -\varepsilon_u t_\Lambda - \frac{2}{3} \varepsilon_u a_\Lambda \int_{t_\Lambda}^t a^{-1} dt.$$

The energy evolution of the N-body system is, of course, fully consistent with the picture of the energy cascade. With the virial kinetic energy K_{pv} continuously cascaded from the smallest scale to the larger scales at a constant rate ε_u , K_{pv} increases linearly with time t . Fig. 18 presents the evolution of kinetic energy on large scales (K_{ph}) and small scales (K_{pv}) in different eras. The simulation data in Figs. 13 and 14 were used to plot the time evolution in Fig. 18 (symbols). The solution in Eq. (88) is also presented for comparison with a constant rate of the cascade $\varepsilon_u = -2.5 \times 10^{-7} \text{m}^2/\text{s}^3$. As expected, the halo kinetic energy

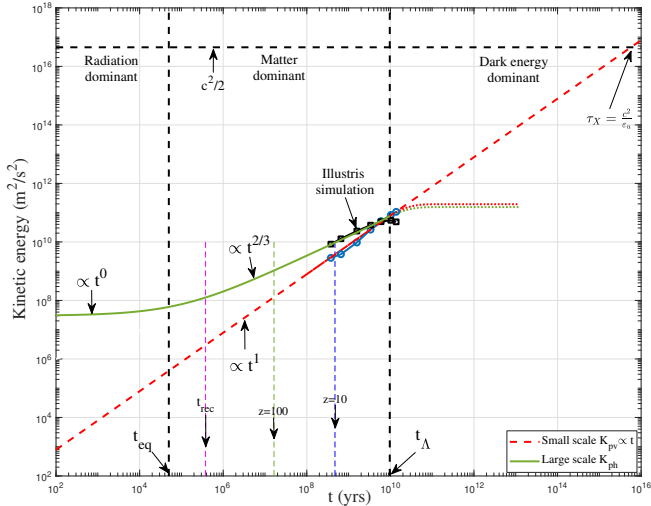


Figure 18. The variation of the specific kinetic energy (energy per unit mass) K_{ph} on large scales and K_{pv} for haloes on small scales with time t (yrs) from Illustris-1-Dark simulation. Solution in Eq. (88) is also presented for comparison with $\varepsilon_u = -2.5 \times 10^{-7} m^2/s^3$. The large-scale kinetic energy K_{ph} is constant in the radiation era and increases in the matter era (i.e., the linear regime with $K_{ph} \propto t^{2/3}$). It slightly decreases at low redshift in the dark energy dominant universe due to the accelerated expansion. Due to intra-halo interactions on small scales (the non-linear regime), the small-scale kinetic energy $K_{pv} = -\varepsilon_u t$ in both radiation and matter eras. In the dark energy era, both kinetic energies level off because of the accelerated expansion and self-limiting effects of dark energy (dotted lines). By assuming that virial velocity cannot exceed the speed of light, a characteristic time $\tau_X = c^2/\varepsilon_u = 10^{16}$ yrs can be obtained. The true lifetime of dark matter can be greater than τ_X .

K_{ph} scales as $\propto t^{2/3}$ due to inter-halo interactions in the linear regime and levels off at low redshift z . In the nonlinear regime, the virial kinetic energy K_{pv} scales as $\propto \varepsilon_u t$ due to the inverse cascade of kinetic energy. This is true for at least up to $z = 0$, as shown in the figure. Now, let us consider the following two scenarios:

i) Dark matter can exist independently of dark energy such that we can consider a matter-dominant universe without dark energy. In this case, the scalings for the halo mass $m_h^* \propto t$ and the kinetic energy $K_{pv} \propto -\varepsilon_u t$ can extend up to a characteristic time τ_X (red dashed line in Fig. 18). By assuming that the speed of particles cannot exceed the speed of light, the characteristic time should be $\tau_X \propto -c^2/\varepsilon_u = 10^{16}$ yrs. Relativistic corrections might be required for a more accurate result. This scenario leads to continuous halo growth, even in the dark energy era, which is not plausible. Dark energy is required to limit and slow down the halo growth.

ii) Dark matter and dark energy have a related and dependent origin. In this case, dark matter must coexist with dark energy. The linear relation $K_{pv} \propto -\varepsilon_u t$ breaks down much earlier than the time τ_X , as dark energy prevents the formation of large haloes. Therefore, virial velocities might level off and never reach the speed of light (dotted lines in Fig. 18). If this is the case, the true lifetime of dark matter can be much greater than $\tau_X = 10^{16}$ yrs. In this scenario, dark energy provides a self-limiting mechanism to slow down the growth of characteristic halo mass m_h^* and the kinetic energy K_{pv} .

In summary, three important observations can be obtained from the energy evolution (Table 2) and the picture of the energy cascade in Figs. 8, 10, 15, 17, and 18, .

(i) Due to the energy cascade in halo mass space, linear evolution

Table 2. Cosmic mass and energy evolution in different eras

Quantity	Symbol	Radiation era	Matter era	Dark energy era
Time	t	a^2	$a^{3/2}$	$\ln a/H_0^*$
Hubble parameter	Ht	$1/2$	$2/3$	$H_0^* t$
Large-scale overdensity	δ	a^0	a^1	a^0
Large-scale KE	K_{ph}	a^0	a^1	a^0
Small-scale KE	K_{pv}	t^1	t^1	t^0
Ratio of A to B (Eq. (85))	A/B	$3/4$	$5/7$	$1/2$
Characteristic halo mass	m_h^*	a^5	$a^{3/2}$	a^0
Total halo mass	M_h	$a^{5/3}$	$a^{1/2}$	a^0
Rate of mass cascade	ε_m	$a^{-1/3}$	a^{-1}	a^{-1}
Rate of energy cascade	ε_u	a^0	a^0	a^{-1}

of kinetic energy $K_{pv} = -\varepsilon_u t$ on small scales can be obtained for both radiation era and matter era. This is also consistent with the cosmic energy equation (Eq. (84)) and the N-body simulations. This is important such that the scaling laws involving ε_u that we will develop in Section 11 are valid in both eras.

(ii) Without dark energy, our universe will stuck in a statistically steady state (matter era of blue circle in Fig. 16), which involves an energy cascade at a constant rate ε_u and a mass cascade at a decreasing rate ε_m . Without dark energy, the kinetic energy K_{pv} and halo mass m_h^* will continuously increase until a characteristic time τ_X in Fig. 18. Since the total amount of dark matter in the universe is fixed, a mechanism is required to limit the growth of m_h^* and K_{pv} . From this perspective, dark energy and dark matter must coexist with each other. Dark energy provides a self-limiting mechanism to limit the growth of dark matter structures.

(iii) Only with the help of dark energy is our universe able to evolve toward the limiting virial equilibrium with a decreasing rate of cascade. The mass and energy cascade only completely vanishes for the system exactly in the limiting virial equilibrium (red star in Fig. 16). Similarly, haloes evolve toward the limiting virial equilibrium with a decreasing rate of cascade. The energy cascade only vanishes in completely virialized haloes. Haloes in their early stage of evolution have a higher rate of cascade than haloes in their late stage of evolution. However, both real and simulated haloes should always have a finite rate of energy cascade (next section).

10 ENERGY CASCADE IN SPHERICAL HALOES

The mass and energy cascade in halo mass space describes the interactions between haloes of different masses. In the radiation and matter eras, the mass and energy cascade established a statistically steady state to continuously release the system energy and maximize the entropy [89]. In the dark energy era, the system approaches the limiting virial equilibrium with a slower mass and energy cascade (Fig. 16). Similarly, there also exists an energy cascade in haloes, while these haloes evolve toward limiting equilibrium. The energy cascade only vanishes for completely virialized haloes. This section quantifies the energy cascade in haloes. The same theory can also be applied to the energy flow in dissipative gases and the associated scaling laws for bulge mass, size, and dynamics [90].

To infer the internal structure of dark matter haloes, we examine the energy cascade in haloes at a given mass m_h . Similarly to the mass and energy cascade in the halo mass space (Sections 7 and 8),

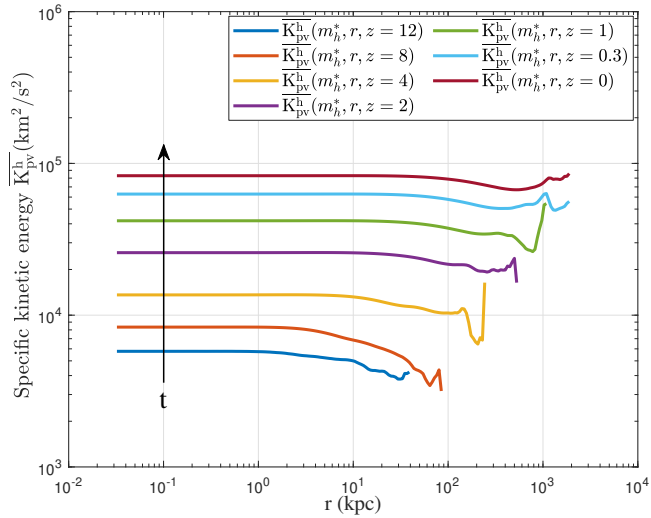


Figure 19. The variation of mean specific kinetic energy $\overline{K_{pv}^h}$ with radial scale r for all haloes of characteristic mass $m_h^*(z)$ at different redshift z . Data is calculated by Eq. (97) and used to compute the rate of energy cascade $\varepsilon(m_h, z)$ in haloes in Fig. 20.

we start by introducing the cumulative functions along the halo radial direction r . The cumulative mass function $\Lambda_m^h(m_h, r, z)$ (similar to Λ_m in Eq. (69)) represents the total mass enclosed above the scale r . This quantity is averaged for all haloes of the same mass m_h

$$\Lambda_m^h(m_h, r, z) = \int_r^\infty \rho_h(m_h, r', z) 4\pi r'^2 dr'. \quad (95)$$

where ρ_h is the mean mass density for all haloes of the same mass.

As usual (see Eq. (74)), next, we decompose the halo particle velocity \mathbf{v}_p into the halo mean velocity, $\mathbf{v}_h = \langle \mathbf{v}_p \rangle_h$, and the velocity fluctuation, \mathbf{v}'_p , that is, $\mathbf{v}_p = \mathbf{v}_h + \mathbf{v}'_p$. Here, \mathbf{v}_h represents the velocity of that halo, that is, the average velocity of all particles in the same halo. Consequently, the total kinetic energy K_p of a given particle can be divided into $K_p = K_{ph} + K_{pv}$. The virial kinetic energy, $K_{pv} = \mathbf{v}'_p{}^2/2$, is the contribution from the velocity fluctuation due to the intra-halo interactions on small scales in the nonlinear regime (Fig. 12). Only this part of the kinetic energy is relevant for the energy cascade in haloes. We will focus on K_{pv} and introduce a cumulative kinetic energy function Λ_{pv}^h for K_{pv}

$$\Lambda_{pv}^h(m_h, r, z) = \int_r^\infty K_{pv} \rho_h(m_h, r', z) 4\pi r'^2 dr'. \quad (96)$$

Next, similarly to the energy cascade in the mass space (Eq. (76)), we introduce the specific kinetic energy on scale r for all haloes of the same mass m_h that reads

$$\overline{K_{pv}^h}(m_h, r, z) = \frac{\Lambda_{pv}^h}{\Lambda_m^h} = \frac{\int_r^\infty K_{pv} \rho_h(m_h, r', z) 4\pi r'^2 dr'}{\int_r^\infty \rho_h(m_h, r', z) 4\pi r'^2 dr'}. \quad (97)$$

Here, $\overline{K_{pv}^h}$ is the specific energy (energy per unit mass) contained on scales above r . Figure 19 plots the variation of the specific kinetic energy $\overline{K_{pv}^h}$ with the scale r at different redshifts for haloes of characteristic mass $m_h = m_h^*$. With $\overline{K_{pv}^h}$ increasing with time, the rate of the energy cascade Π_{pv}^h along the halo radial direction is defined as

$$\Pi_{pv}^h(m_h, r, z) = -\frac{\partial}{\partial t} \left(\overline{K_{pv}^h} \right) = -\frac{\partial}{\partial t} \left(\frac{\Lambda_{pv}^h}{\Lambda_m^h} \right). \quad (98)$$

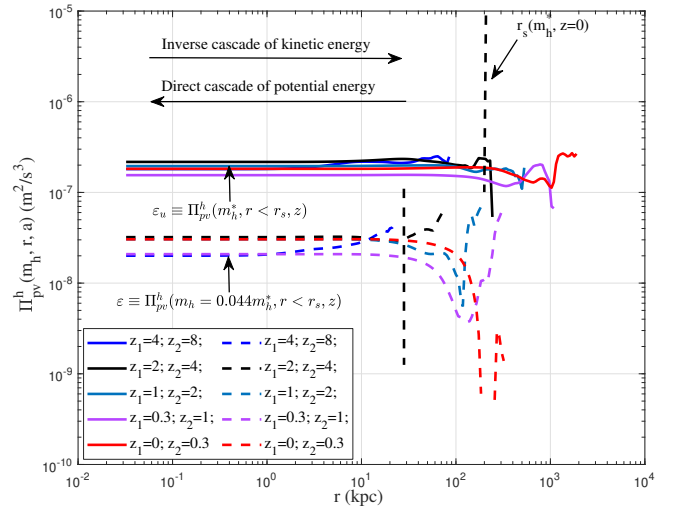


Figure 20. The variation of the rate of energy cascade $\Pi_{pv}^h(m_h, r, z)$ (Eq. (77)) with radial scale r at different redshifts z for haloes of characteristic mass $m_h^*(z)$ and $m_h = 0.044m_h^*(z)$. A scale-independent (independent of r) constant rate of $\varepsilon \equiv \Pi_{pv}^h(r < r_s)$ can be identified for an inverse cascade of virial kinetic energy K_{pv} from halo center to larger scales. There also exists a simultaneous direct cascade of potential energy from large to the smallest scale at a rate of $-7/5\varepsilon$ (see Eq. (88)). For haloes with characteristic mass m_h^* , the rate of energy cascade $\varepsilon(m_h^*, z) \equiv \varepsilon_u \approx 10^{-7} m^2/s^3$.

In a certain range of scales $r < r_s^*$ (inner haloes), the characteristic time scale on the small scale is very fast compared to the time scale on the large scale. The small-scale motion does not feel the slow large-scale motion directly, except through the rate of energy flux ε . Therefore, when a statistical equilibrium is established, similarly to the energy cascade in the halo mass space, we expect a constant $\varepsilon(m_h, z)$ that is independent of scale r in the range $r < r_s^*$, i.e.,

$$\varepsilon((m_h, z)) \equiv \Pi_{pv}^h(m_h, r, z) = -\frac{\partial \overline{K_{pv}^h}}{\partial t} \quad \text{for } r < r_s^*. \quad (99)$$

Figure 20 plots the variation of the parameter $\varepsilon(m_h, z)$ using Eq. (97) and the kinetic energy $\overline{K_{pv}^h}$ in Fig. 19. In this figure, a scale-independent parameter ε can be clearly observed below a characteristic size r_s^* , usually the scale radius. The key parameter ε increases with the halo mass m_h and the redshift z . For haloes with characteristic mass m_h^* , the rate of energy cascade $\varepsilon(m_h^*, z) \equiv \varepsilon_u$.

Similarly, we can calculate the rate of the energy cascade for haloes of different masses. Using the data in Fig. 20, Fig. 21 plots the variation of $\varepsilon(m_h, z)$ with the halo mass m_h and the redshift z . The figure shows that $\varepsilon \propto m_h^{2/3}$ and increases with redshift z ,

$$\varepsilon(m_h, z) = \varepsilon_u v = \varepsilon_u (m_h/m_h^*)^{2/3} \propto m_h^{2/3} a^{-1}, \quad (100)$$

where $\varepsilon_u \equiv \varepsilon(m_h^*, z)$ is the rate of energy flow in haloes of characteristic mass m_h^* . The peak height parameter of dark matter haloes is defined as $v = (m_h/m_h^*)^{2/3}$ [87]. The rate of energy cascade decreases with the halo mass and time as $\varepsilon \propto m_h^{2/3} a^{-1}$ while evolving towards the limiting equilibrium. We have $\varepsilon = 0$ only in fully virialized haloes, a limiting state that real haloes can never reach.

11 SCALING LAWS AND HALO DENSITY PROFILES

Scaling laws are well known to be associated with the energy cascade phenomenon in turbulence [63, 38]. In this section, we focus on the

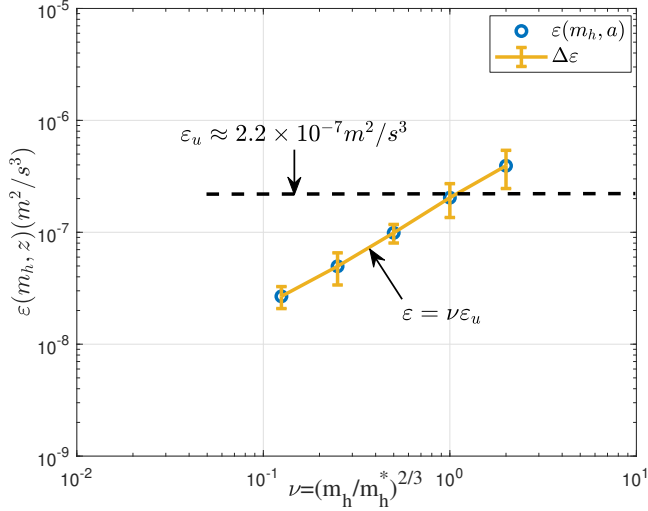


Figure 21. The variation of the rate of energy cascade $\varepsilon(m_h, z)$ (Eq. (77)) with halo mass m_h at different redshifts z in terms of the dimensionless peak height parameter $\nu = (m_h/m_h^*)^{2/3}$. A scale-independent constant rate of ε_u can be identified at $\nu = 1$ or $m_h = m_h^*$. That rate is also relatively independent of time and is around $-2.5 \times 10^{-7} m^2/s^3$ (also see Fig. 18).

scaling laws related to the energy cascade in spherical haloes and their effects on halo density profiles, which can be used to infer the dark matter mass and properties.

We first consider the relevant scaling laws. Here, two perspectives are presented that may lead to these scaling laws. In the first perspective, similar to the smallest two-particle haloes (Eq. (56)), the rate of the energy cascade in haloes of mass m_h^* can be written as:

$$-\varepsilon_u \propto v_r^3/r = v_r^2/(r/v_r) \quad \text{or} \quad v_r^2 \propto (\varepsilon_u r)^{2/3}, \quad (101)$$

where ε_u is the rate of cascade in these haloes (Fig. 20), v_r is the characteristic velocity on scale r , and $t_r = r/v_r$ is the time scale. This states that the kinetic energy v_r^2 on the scale r is cascaded to large scales during a turnaround time t_r . The two-thirds law ($v_r^2 \propto (\varepsilon_u r)^{2/3}$) can be directly validated by N-body simulations [86]. On scale r , the virial theorem reads

$$v_r^2 \propto \frac{G m_r}{r}, \quad (102)$$

where m_r is the mass enclosed within the scale r . Combining Eq. (101) with the virial theorem in Eq. (102), we obtain a five-thirds law for halo mass $m_r \propto \varepsilon_u^{2/3} G^{-1} r^{5/3}$ that can also be confirmed by Illustris simulations [86]. Similarly, the density enclosed within scale r should follow $\rho_r \propto m_r/r^3 \propto \varepsilon_u^{2/3} G^{-1} r^{-4/3}$, that is, a four-thirds law for the halo density. We start with the two-thirds law,

$$-\lambda_u \varepsilon_u = \frac{2v_r^2}{r} v_r = \frac{2v_r^2}{r/v_r} = \frac{2v_r^2}{t_r}, \quad (103)$$

where λ_u is just a dimensionless numerical constant on the order of unity. Combining Eq. (103) with the virial theorem in Eq. (102), we can easily obtain the scaling laws for mass scale m_r (mass enclosed within r), the density scale ρ_r (mean density of the halo enclosed within r), velocity scale v_r (circular velocity at r), time t_r , and kinetic energy v_r^2 , all determined by ε_u , G and scale r :

$$\begin{aligned} m_r &\propto \alpha_r \varepsilon_u^{2/3} G^{-1} r^{5/3}, & \rho_r &\propto \beta_r \varepsilon_u^{2/3} G^{-1} r^{-4/3}, \\ v_r &\propto (-\varepsilon_u r)^{1/3}, & t_r &\propto (-\varepsilon_u)^{-1/3} r^{2/3}, \\ v_r^2 &\propto (\varepsilon_u G m_r)^{2/5}, \end{aligned} \quad (104)$$

where $\alpha_r \approx 5.28$ and $\beta_r \approx 1.26$ are two constants that can be determined by data fitting. The 2/5 scaling between kinetic energy v_r^2 and halo mass m_r was also plotted in Fig. 14 and is in good agreement with the Illustris simulation. These scaling laws are for haloes with characteristic mass m_h^* and constant rate of cascade ε_u . For haloes with other masses, we replace ε_u by a mass-dependent rate of the cascade ε in Eq. (100). For example, the inner density for the haloes of mass m_h should read (-4/3 law)

$$\rho_r(r, m_h, z) = \beta_r \varepsilon^{2/3} G^{-1} r^{-4/3} = \beta_r \varepsilon_u^{2/3} G^{-1} r^{-4/3} \left(\frac{m_h}{m_h^*(z)} \right)^{4/9}. \quad (105)$$

The model predicts the halo density $\rho_h(r) \propto m_h^{4/9} a^{-2/3}$ for halos of different masses with $m_h^* \propto a^{3/2}$ (Table 2). In addition, scaling laws in Eq. (104) predicts a limiting density slope of $\gamma = -4/3$ in the halo core region. Therefore, the inner structure of the haloes can be determined by the energy cascade in the haloes.

We next focus on the halo density profile. The well-known core-cusp problem describes the discrepancy between cuspy halo density predicted by cosmological CDM-only simulations and core density from observations. The predicted halo density exhibits a cuspy inner density $\rho \propto r^\gamma$ with a wide range of γ between -1.0 and -1.5. The NFW profile is a very popular model with a density slope of $\gamma = -1.0$ [52]. The density slopes of the simulated haloes are also found to be $\gamma > -1.0$ [53], $\gamma = -1.2$ [18], and $\gamma = -1.3$ [28, 47]. There seems to be no consensus on the exact value of the asymptotic slope γ and no solid theory for the density slope γ .

From the mass continuity equation for a spherical halo [86], we can demonstrate that the density slope γ is highly dependent on the mean radial flow $u_r(r, t)$ (flow along the radial direction) as

$$\gamma \approx \frac{\nu}{1-\mu} - 3, \quad \nu = \frac{\partial \ln m_r(r_s)}{\partial \ln r_s}, \quad \mu = \frac{u_r t}{r} \left/ \frac{\partial \ln r_s}{\partial \ln t} \right. \quad (106)$$

Here, r_s is the scale radius where the logarithmic slope is -2, and $m_r(r_s)$ is the total mass enclosed within the scale radius r_s . The parameter μ represents the effect of the radial flow (u_r). A higher radial flow u_r or greater μ leads to a smaller γ and a flatter density. The parameter $\nu = 5/3$ represents the effect of the energy cascade, as we can find from the 5/3 law between m_r and r in Eq. (104).

Based on the effects of radial flow and energy cascade, we will consider the following scenarios:

(i) Individual haloes with both non-zero radial flow and non-vanishing energy cascade ($u_r \neq 0$, $\varepsilon \neq 0$). Most simulated haloes are non-equilibrium dynamic objects that have both a nonzero radial flow and a non-vanishing energy cascade. The density slopes of individual haloes depend on both the radial flow and the mass accretion of each halo, as shown in Eq. (106). This may be the reason for the wide variety of density slopes γ for simulated haloes. In previous work, we have analytically derived the halo density profiles based on the concept of a mass and energy cascade [87]. Simulated haloes with different density slopes can generally be modeled by a double- γ density profile

$$\rho_h(r, t) = \rho_s(t) \left(\frac{r}{r_s} \right)^{\frac{\alpha}{\beta} - 2} \exp \left(\frac{1}{\beta} \left(1 - \left(\frac{r}{r_s} \right)^\alpha \right) \right), \quad (107)$$

where $\rho_s(t)$ is the density at scale radius $r_s(t)$. This four-parameter double- γ density profile (ρ_s , r_s , α , and β in Eq. (107)) reduces to the standard three-parameter Einasto profile with $\alpha = 2\beta$.

(ii) Haloes with vanishing radial flow and non-vanishing energy cascade ($u_r = 0$ and $\varepsilon \neq 0$). Individual haloes have random radial

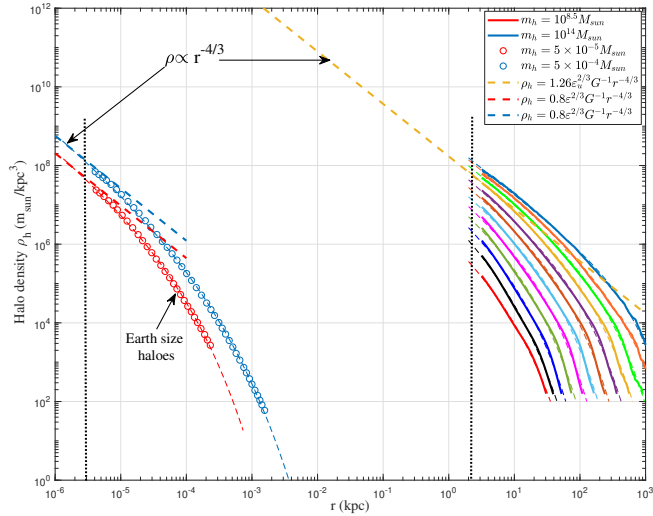


Figure 22. The density profiles from cosmological simulations for haloes of different mass at $z = 0$. The solid lines present the average density profiles for all haloes with a mass between $10^{\pm 0.1} m_h$ from the Illustris simulation for galactic haloes of mass $m_h = [10^{8.5} 10^{14}] M_\odot$. The symbols present two Earth-size simulated haloes [77]. The thin dashed lines present the double- λ density profile from Eq. (108). The thick dashed (straight) lines represent the $-4/3$ scaling law for haloes of mass m_h with the rate of energy cascade $\varepsilon \propto m_h^{2/3}$ (Eq. (109)), and for haloes of characteristic mass $m_h^*(z=0)$ (Eq. (110)). The dotted lines indicate the softening length. The figure demonstrates the $-4/3$ law from the concept of energy cascade for the density profiles of haloes of different sizes over 20 orders of magnitude. The density profiles of haloes with mass $m_h^*(z)$ at different redshifts z are presented in Fig. 24.

flow. However, in N-body simulations, we can average out radial flow by constructing composite haloes of a given mass m_h from all haloes of the same mass. This is what we did in Section 10, where relevant quantities are averaged for all haloes with the same mass. For these composite haloes, the radial flow vanishes, and we only have the effect of the energy cascade ($\mu = 0$ and $\nu = 5/3$ in Eq. (106)) such that the inner density slope $\gamma = -4/3$. The inner halo region with vanishing radial flow or $u_r = 0$ is also expected from the stable clustering hypothesis; that is, there is no net stream motion in physical coordinate along the radial direction [50, 88]. For haloes with no radial flow, we would expect an inner density with a slope of $-4/3$. The corresponding double-density profile (let $\alpha/\beta = 2/3$ in Eq. (107)) should read [87]

$$\rho_h(r, m_h, z) = \beta_r \varepsilon^{2/3} G^{-1} r_s^{-4/3} \left(\frac{r}{r_s} \right)^{-4/3} \exp \left[-\frac{1}{\beta} \left(\frac{r}{r_s} \right)^{2/3} \right], \quad (108)$$

$$\varepsilon(m_h, z) = (m_h/m_h^*(z))^{2/3} \varepsilon_u,$$

where $\beta_r \approx 1$ is an amplitude parameter, β is a shape parameter, and r_s is the scale radius. Here, $\varepsilon_u = -4.6 \times 10^{-7} m^2/s^3$ is the rate of the energy cascade for haloes with characteristic mass $m_h^*(z)$. While $\varepsilon(m_h, z)$ is the rate of the energy cascade in haloes of any mass m_h (Eq. (100)). For small r , the inner density reduces to (recovers the scaling law in Eq. (105))

$$\rho_h(r, m_h, z) = \beta_r \varepsilon^{2/3} G^{-1} r^{-4/3} \quad \text{for } r \rightarrow 0, \quad (109)$$

where the redshift dependence is incorporated into ε , which is dependent on the characteristic mass $m_h^*(z)$ (Eq. (108)). For haloes of characteristic mass $m_h^*(z)$, there exists a small-scale permanence for the halo density, i.e., the density profiles at different redshifts z

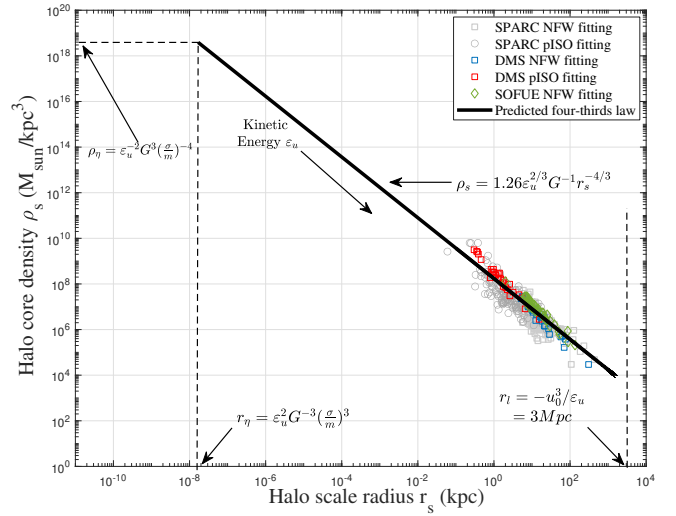


Figure 23. The variation of halo core density ρ_s with the halo scale radius r_s from galaxy rotation curves. Each data represents the result for a given galaxy. The predicted $-4/3$ law in Eq. (104) is also plotted for comparison (solid black line). The good agreement confirms the predicted scaling laws from the energy cascade. For self-interacting dark matter model with a cross-section σ/m , there exists the smallest structure with a size r_η and a maximum density ρ_η determined by ε_u , G , and σ/m (Table 5). The largest halo size $r_l = -u_0^3/\varepsilon_u$ is determined by the velocity dispersion u_0 and ε_u .

converge to a time-unvarying scaling,

$$\rho_h(r, m_h^*, z) \equiv \rho_h(r) = \beta_r \varepsilon_u^{2/3} G^{-1} r^{-4/3} \quad \text{for } r \rightarrow 0. \quad (110)$$

The small-scale permanence is shown and discussed in Fig. 24.

(iii) The last scenario is completely virialized haloes with both vanishing radial flow and vanishing energy cascade ($u_r = 0$ and $\varepsilon = 0$). This is the limiting virial equilibrium state (simulated or real) haloes evolve toward but can never reach. The $-4/3$ density slope should still be good in this limiting state.

To validate the predicted scaling laws, we first present the density profiles from cosmological simulations for haloes of different masses m_h at $z = 0$. In Fig. 22, the solid lines present the average halo density profiles for all haloes with a mass between $10^{\pm 0.1} m_h$ from the Illustris simulation, where $10^8 M_\odot < m_h < 10^{14} M_\odot$. The symbols present two Earth-size simulated haloes with a mass of $5 \times 10^{-5} M_\odot$ and $5 \times 10^{-4} M_\odot$, respectively [77]. The thin dashed lines present the double- λ density profile from Eq. (108). The thick dashed (straight) lines represent the $-4/3$ scaling laws for haloes of mass m_h that involve the rate of cascade $\varepsilon \propto m_h^{2/3}$ (Eq. (109)). Here, $\varepsilon = \varepsilon_u$ for haloes of characteristic mass m_h^* (Eq. (110)). The figure demonstrates the $-4/3$ law that we obtained from the concept of energy cascade. That scaling was in agreement with the density profiles of haloes of more than 20 orders of magnitude.

Observational evidence of the predicted scaling laws also exists. The four-thirds law $\rho_r(r) \propto r^{-4/3}$ for the halo mass density enclosed within the scale r can also be directly compared against data from galaxy rotation curves (Fig. 23). Important information for dark matter haloes can be extracted from galaxy rotation curves by decomposing them into contributions from different mass components. Once the halo density model is selected, the scale radius r_s and the mean density ρ_s within r_s can be rigorously obtained by fitting the decomposed rotation curve. In this work, for pseudo-isothermal (pISO)

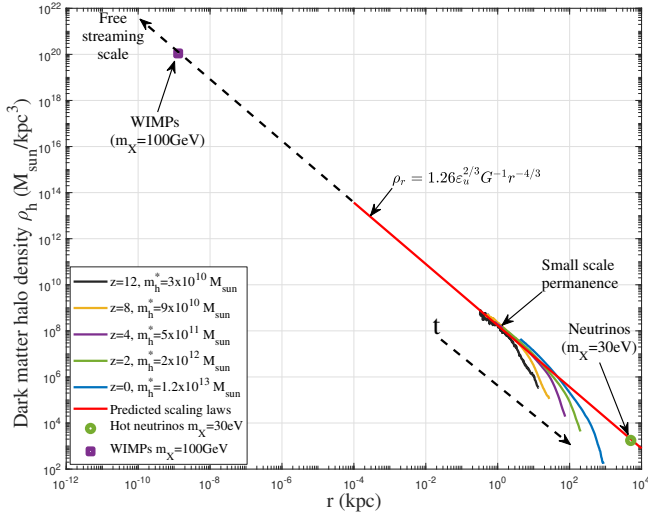


Figure 24. The redshift evolution of halo density profiles for haloes with a characteristic mass $m_h^*(z)$. Density profiles for haloes with other masses (from the galaxy cluster to the Earth size) are presented in Fig. 22. This figure demonstrates the small-scale permanence, i.e., the density profiles for haloes with a characteristic mass $m_h^*(z)$ at different redshifts z all collapse at a small scale r onto the predicted time-unvarying scaling (solid red line from Eq. (110)). Due to the time and scale-independent rate of the cascade ε_u , the $-4/3$ scaling should extend to smaller scales (or earlier time) until reaching the smallest scale (or the formation time of the smallest structures) that depends on the nature of dark matter (Sections 2). The halo mass, density, size, and formation time at the smallest scale are calculated in Eq. (111). Two examples, hot neutrinos (green dot) and WIMPs (purple square) are plotted in the same figure and listed in Table 3.

models [2] and NFW density models [52], three different sources of rotation curves are used to extract r_s and density ρ_s within r_s ,

- (i) SPARC (Spitzer Photometry & Accurate Rotation Curves) including 175 late-type galaxies [41, 42];
- (ii) DMS (DiskMass Survey) including 30 spiral galaxies [45];
- (iii) SOFUE (compiled by Sofue) with 43 galaxies [69].

Figure 23 presents the variation of the halo core density ρ_s with the scale radius r_s obtained from the galaxy rotation curves (square and circle symbols). Each symbol represents data from a single galaxy. The four-thirds law (Eq. (104)) is also plotted (black line) with constants $\beta_r = 1.26$ (equivalent to $\alpha_r = 5.28$) obtained from these data. From this figure, dark matter haloes from galaxy rotation curves follow the $-4/3$ law across six orders of halo mass.

Finally, we are especially interested in the redshift evolution of haloes with a characteristic mass $m_h^*(z)$, which is representative. Figure 24 shows the time evolution of the average density profiles for all haloes with characteristic masses $m_h^*(z)$ from Illustris simulations. By averaging out the radial flow, the energy cascade should give rise to a slope of $\gamma = -4/3$ (Eq. (106)). At higher redshifts, dark matter haloes tend to be smaller with higher density. The density profiles of all dark matter haloes converge to the predicted time-unvarying scaling (solid red line) from Eq. (110), i.e., the small-scale permanence that can be confirmed by N-body simulations.

The $-4/3$ scaling law in Fig. 24 should extend to smaller and smaller scales until the scale of the smallest halo. That scale can be the free streaming scale, which is dependent on the nature and mass of dark matter particles (Sections 2). The heavier particles have a smaller free streaming scale. For sufficiently heavy DM particles of mass $m_{Xc} \approx 10^{12}$ GeV, the free streaming mass can be comparable

Table 3. Dark matter particle candidates and the free streaming scale

Quantities	Symbol	Hot neutrinos	WIMPs	X particle
Particle mass	m_X	30eV	100GeV	10^{12} GeV
Free streaming	M_{fs}	$10^{15}M_\odot$	$10^{-6}M_\odot$	10^{12} GeV
Size	r_{fs}	5Mpc	10^{-9} kpc	10^{-13} m
Density	ρ_{fs}	10^{-25} kg/m ³	10^{-8} kg/m ³	10^{23} kg/m ³
Formation time	t_{fs}	10^{11} yrs	300yrs	10^{-6} s

to the particle mass (Fig. 2) such that the $-4/3$ scaling can extend to the scale of the smallest structure (two-particle haloes). Since smaller structures were formed earlier (as early as the radiation era in Section 4), extending to smaller scales is equivalent to extending to an earlier time. For dark matter candidates with known free streaming mass M_{fs} , scaling laws in Eq. (104) can be used to calculate the relevant quantities for the smallest structure of the free streaming scale,

$$\begin{aligned}
 r_{fs} &= \alpha_r^{-3/5} \varepsilon_u^{-2/5} G^{3/5} M_{fs}^{3/5}, \\
 \rho_{fs} &= \beta_r \alpha_r^{4/5} \varepsilon_u^{6/5} G^{-9/5} M_{fs}^{-4/5}, \\
 t_{fs} &= \varepsilon_u^{-3/5} G^{2/5} M_{fs}^{2/5},
 \end{aligned} \tag{111}$$

where r_{fs} , ρ_{fs} , and t_{fs} are the size, density, and formation time of the smallest haloes with a free streaming mass M_{fs} .

In Fig. 24, two examples are presented, that is, the hot neutrinos with $M_{fs} = 10^{15}M_\odot$ (green dot) and standard WIMPs with $M_{fs} = 10^{-6}M_\odot$ (purple square). Table 3 lists the relevant quantities calculated for the smallest halo structure formed by three dark matter candidates. The particle X with critical mass $m_X = M_{fs} = 10^{12}$ GeV was also listed, which has been extensively discussed in Sections 2 and 4 (Eq. (55)). Obviously, the cold dark matter (WIMPs and X) leads to much smaller structures formed in the earlier universe. Finally, at what scale should the $-4/3$ scaling stop operating strongly suggests the nature of dark matter particles (Section 12).

12 DARK MATTER PARTICLE MASS AND PROPERTIES

In this section, we attempt to estimate the mass and properties of the cold dark matter particles from the established scaling laws in Section 11. Since the rate of the energy cascade ε_u in Eq. (89) is both scale- and time-independent, the scaling laws should extend to the smallest scale (Fig. 24) and the earliest time when the smallest structure was formed, as early as in the radiation era (Section 4). Here, we consider X particles with a mass $m_X \geq m_{Xc}$, or the free streaming mass is less than the particle mass (Fig. 2). In this case, the free streaming scale is not relevant, and the smallest structures formed can be two-particle haloes. The highest possible density of the two-particle haloes cannot be infinite and is limited by the uncertainty principle such that the scaling laws may extend to a scale where quantum effects become important. For particles with a mass $m_X \ll m_{Xc}$, the smallest haloes are determined by the free streaming mass (Eq. (111)).

Assuming that gravity is the only interaction between unknown dark matter particles (traditionally denoted by X), the only dominant physical constants on the smallest scale are the reduced Planck constant \hbar (the quantum effect), the gravitational constant G (the gravitational interactions) and the rate of energy cascade ε_u . Without involving complex quantum field theory for a more rigorous treatment, a formal dimensional analysis often provides significant insights. Any physical quantities Q on that scale can be expressed as $Q = \varepsilon_u^x G^y \hbar^z$, where x , y , and z can be uniquely determined by

dimensional analysis. Examples are the mass and length scales,

$$m_X = \left(-\varepsilon_u \hbar^5 G^{-4}\right)^{\frac{1}{9}} \quad (112)$$

and

$$l_X = \left(-\varepsilon_u^{-1} G \hbar\right)^{\frac{1}{3}}. \quad (113)$$

Alternatively, the same results can be obtained from a refined treatment to couple relevant physical laws on the smallest scale. This may offer a complete view than a simple dimensional analysis. Let us consider two X particles on the smallest scale with separation $2r_X = l_X$ in the rest of the center of mass of two particles. On that scale, three relevant physics are as follows:

$$m_X V_X \cdot l_X / 2 = \hbar, \quad (114)$$

$$G m_X / l_X = 2V_X^2, \quad (115)$$

$$2V_X^3 / l_X = a_X \cdot v_X = -\lambda_u \varepsilon_u, \quad (116)$$

where Eq. (114) is from the uncertainty principle for momentum and position if X particles exhibit wave-particle duality. Equivalently, we can also treat $l_X/2$ as the de Broglie wavelength of the matter wave of X particle. Equation (115) is from the virial theorem for the potential energy (V) and the kinetic energy (T), that is, $2T = -V$. Here, V_X is the relative velocity between two particles due to their interactions and contributes to the small-scale virial kinetic energy K_{pv} . The last equation (116) is from the two-thirds (2/3) law in Eq. (103) associated with the energy cascade in dark matter reflecting the "uncertainty" principle between particle acceleration and velocity [86]. Since the energy cascade rate ε_u is both scale- and time-independent, we may extend the 2/3 law down to the smallest scale for dark matter particle properties. By this approach, the dark matter particle properties on small scales are consistent with the established scaling laws for dynamics of dark matter haloes on large scales. With the following values for three constants,

$$\begin{aligned} \varepsilon_u &= -4.6 \times 10^{-7} m^2/s^3, \\ \hbar &= 1.05 \times 10^{-34} kg \cdot m^2/s, \\ G &= 6.67 \times 10^{-11} m^3/(kg \cdot s^2), \end{aligned} \quad (117)$$

Complete solutions of Eqs. (114), (115), and (116) can be obtained (with $\lambda_u = 1$), relevant quantities on the X scale are (Fig. 25),

$$m_X = \left(-\frac{256\lambda_u \varepsilon_u \hbar^5}{G^4}\right)^{\frac{1}{9}} = 1.62 \times 10^{-15} kg \approx 10^{12} GeV, \quad (118)$$

$$l_X = \left(-\frac{2G\hbar}{\lambda_u \varepsilon_u}\right)^{\frac{1}{3}} = 3.12 \times 10^{-13} m, \quad (119)$$

$$t_X = \frac{l_X}{V_X} = \left(-\frac{32G^2\hbar^2}{\lambda_u^5 \varepsilon_u^5}\right)^{\frac{1}{9}} = 7.51 \times 10^{-7} s,$$

$$V_X = \left(\frac{\lambda_u^2 \varepsilon_u^2 \hbar G}{4}\right)^{\frac{1}{9}} = 4.16 \times 10^{-7} m/s, \quad (120)$$

$$a_X = \left(-\frac{4\lambda_u^7 \varepsilon_u^7}{\hbar G}\right)^{\frac{1}{9}} = 1.11 m/s^2.$$

Note that the solutions of mass m_X and length scale l_X agree with those obtained from a formal dimensional analysis in Eqs. (112) and (113). The predicted particle mass is much heavier than standard

WIMPs and is of the same order as the critical mass m_{Xc} in Eq. (14). Therefore, the corresponding free streaming mass for particles of this mass should be comparable to the particle mass, allowing us to extend the scaling laws to the particle mass scale.

The time scale t_X (formation time of the smallest structures) is close to the characteristic time for weak interactions ($10^{-6} \sim 10^{-10} s$). In contrast, the length scale l_X is greater than the characteristic range of strong interactions ($\sim 10^{-15} m$) and weak interactions ($\sim 10^{-18} m$). The "thermally averaged cross section" of X particle is around $l_X^2 V_X = 4 \times 10^{-32} m^3/s$. This is on the same order as the cross-section required for the correct abundance of today via thermal production ("WIMP miracle"), where $\langle\sigma v\rangle \approx 3 \times 10^{-32} m^3 s^{-1}$. The "cross section σ/m " for X particle is extremely small, i.e. $l_X^2/m_X = 6 \times 10^{-11} m^2/kg$, i.e., a fully collisionless dark matter. In addition, a new constant μ_X (the scale for the rate of energy dissipation) can be introduced,

$$\begin{aligned} \mu_X &= m_X a_X \cdot V_X = F_X \cdot V_X = -m_X \varepsilon_u \\ &= \left(-\frac{256\varepsilon_u^{10}\hbar^5}{G^4}\right)^{\frac{1}{9}} = 7.44 \times 10^{-22} kg \cdot m^2/s^3 \end{aligned} \quad (121)$$

which is a different representation of ε_u . In other words, the fundamental physical constants on the smallest scale can be \hbar , G , and the constant μ_X . Consequently, an important energy scale is set by

$$E_X = \mu_X t_X / 4 = \hbar / t_X = \sqrt{\hbar \mu_X} / 2 = 0.87 \times 10^{-9} eV. \quad (122)$$

This energy scale is the binding energy of two X particles in the ground state (Eq. (55)). It is equivalent to a Compton wavelength of 1.4 km or a frequency of 0.2 MHz. This can be relevant to the possible dark "radiation" (Section 14).

The relevant mass density is around $m_X/l_X^3 \approx 5.33 \times 10^{22} kg/m^3$, much higher than the nuclear density of the order of $10^{17} kg/m^3$ (Fig. 26). This density is about $32\pi^2$ times the background density of the universe at the formation time t_X , in agreement with the spherical collapse model. The relevant pressure scale is

$$P_X = \frac{m_X a_X}{l_X^2} = \frac{8\hbar^2}{m_X} \rho_{nX}^{5/3} = 1.84 \times 10^{10} Pa, \quad (123)$$

which sets the highest pressure or the possible "degeneracy" pressure of dark matter that stops further gravitational collapse. Equation (123) is an analog of the degeneracy pressure of the ideal Fermi gas, where $\rho_{nX} = l_X^{-3}$ is the number density of the particle X . With today's dark matter density around $2.2 \times 10^{-27} kg/m^3$ and local density $7.2 \times 10^{-22} kg/m^3$, the mean separation between X particles is about $l_u \approx 10^4 m$ in the entire universe and $l_c \approx 130 m$ locally.

In summary, Fig. 25 presents a detailed interpretation. Different combinations of three relevant physics leads to some interesting findings in Fig. 25. Combining Eq. (114) with Eq. (115) leads to the black dashed line in Fig. 25, a relation between the mass and size of the particles ($m_r \propto r^{-1/3}$). A similar relation can also be obtained from the Schrödinger-Newton equation, a nonlinear modification of the Schrödinger equation with Newtonian gravity for self-interaction. This line represents the boundary below which quantum effects are important and dominant over gravity.

Combining Eq. (116) with Eq. (115) leads to the five-thirds ($m_r \propto r^{3/5}$) law between the halo mass and the halo size (see Eq. (104) for the 5/3 law), the blue dashed line in Fig. 25. Dark matter haloes from galaxy rotation curves also fall on the same line. This line represents the dynamics of dark matter haloes on large scales. To find the dark matter particle properties that are consistent with the dynamics of dark matter haloes on large scales, extending the five-thirds law (blue

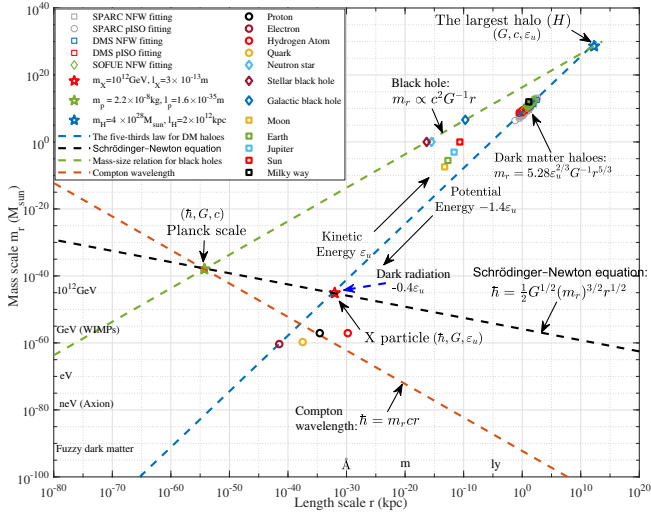


Figure 25. The variation of mass scale m_r and size scale r for cold dark matter particle properties. This figure estimates the cold dark matter particle properties on small scales that are consistent with the dynamics of dark matter haloes on large scales. Collisionless dark matter haloes follow the scaling $m_r \propto r^{5/3}$ (the blue dashed line for the five-thirds law in Eq. (104)) due to the energy cascade at a constant rate ε_u for kinetic energy and $-1.4\varepsilon_u$ for potential energy (Eq. (88) and Fig. 17). Dark matter haloes from different surveys of galaxy rotation curves in Fig. 23 follow the five-thirds law. The black dashed line represents the combined quantum and gravitational effects of Eqs. (114) and (115). The green dashed line gives the mass of black holes (BHs) at a given size r (Schwarzschild radius) from stellar to galactic BHs, i.e., the maximum mass at any given r . By extending the five-thirds law (blue dashed line) for dark matter haloes to the smallest scale (intersecting the black dashed line), the red star represents the cold dark matter particles (X) with predicted mass m_X and size l_X from Eqs. (112) and (113) (also see Table 4). By extending the five-thirds law (blue dashed line) for dark matter haloes to the largest scale to intersect the green dashed line (the blue star), we will obtain the largest scales (the H scale) of halo size (l_H), mass (m_H), and time (t_H or DM lifetime τ_X in Eq. (124)) (see table 4). The green star represents the Planck scale. For comparison, the mass and size of some particles and astronomical objects are also shown.

Table 4. Physical quantities on the X scale, the H scale and the Planck scale

Scales	The X scale	The H scale	The Planck scale
Length	$l_X = \left(-\frac{G\hbar}{\varepsilon_u}\right)^{1/3}$	$l_H = -\frac{c^3}{\varepsilon_u}$	$l_P = \sqrt{\frac{\hbar G}{c^3}}$
Time	$t_X = \left(-\frac{G^2\hbar^2}{\varepsilon_u^5}\right)^{1/9}$	$t_H = -\frac{c^2}{\varepsilon_u}$	$t_P = \sqrt{\frac{\hbar G}{c^3}}$
Mass	$m_X = \left(-\frac{\varepsilon_u\hbar^5}{G^4}\right)^{1/9}$	$m_H = -\frac{c^5}{\varepsilon_u G}$	$m_P = \sqrt{\frac{\hbar c}{G}}$

dashed) to the smallest scale will intersect the black dashed line, i.e., the red star in Fig. 25, where quantum effect becomes relevant, and scaling laws might stop operating. This should be the scale of the X particle (the X scale). We show that the free streaming mass is comparable to the particle mass at this scale (Eq. (14)).

Finally, the mass of black holes at a given size r (Schwarzschild radius) is plotted as a green dashed line ($m_r \propto r$). This is the maximum mass m_r on a given scale r . Extending the green dashed line to intersect the blue dashed line, i.e., the blue star leads to the largest scale (the H scale) of dark matter haloes. This is, of course, the largest possible scale of dark matter haloes that can be reached during the lifetime of dark matter. The black dashed line intersects the green dashed line on the Planck scale.

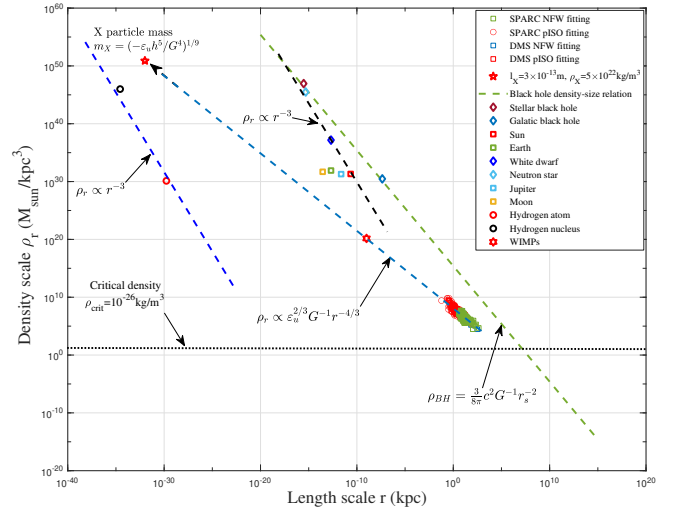


Figure 26. The variation of density scale ρ_r with size scale r for cold dark matter particle properties. By extending the four-thirds law in Fig. 23 for dark matter haloes to the smallest scale where quantum effects are dominant, the red star (the X scale) represents the cold DM particles with predicted density ρ_X and size l_X from Eqs. (112) and (113). Collisionless dark matter haloes follow the scaling $\rho_r \propto r^{-4/3}$ due to the energy cascade at a constant rate ε_u . The densities of sun, dwarf, neutron star, and stellar black holes follow the scaling $\rho_r \propto r^{-3}$ reflecting the formation of stellar black holes from the collapse of massive stars. The density of black holes (ρ_{BH}) as a function of Schwarzschild radius (r_s) follows $\rho_{BH} \propto r_s^{-2}$, extending from stellar to galactic black holes. WIMPs from Table 3 is also reported (red hexagram).

In this plot, three key scales (Table 4) are determined by different constants, i.e., the green star for the Planck scale (\hbar , G , and c), the red star for the smallest halo scale or the DM particle scale X (\hbar , G , and ε_u), and the blue star for the largest halo scale H (G , c , and ε_u). Table 4 provides relevant quantities on three key scales. For comparison, the mass and actual size of some typical particles and astronomical objects are also presented in the same figure.

Similarly, Figure 26 illustrates the variation of the density scale ρ_r with size r . By extending the four-thirds law in Fig. 23 to the smallest scale where the quantum effect becomes dominant, we obtain the red star in Fig. 26 for cold DM particles with predicted mass m_X and size l_X from Eqs. (112) and (113). The density and size of some typical particles and astronomical objects are also included for comparison. As expected, the density of the sun, dwarf, neutron star, and stellar black hole follows the scaling $\rho_r \propto r^{-3}$, while the density of black holes (ρ_{BH}) computed using the Schwarzschild radius (r_s) follows a simple scaling $\rho_{BH} \propto r_s^{-2}$. Thus, Fig. 26 displays three distinct scaling laws for density-size relations of different objects reflecting different operating physics, i.e. $\rho_r \propto r^{-4/3}$ for dark matter haloes, $\rho_r \propto r^{-3}$ for the formation of stellar black holes, and $\rho_r \propto r^{-2}$ for black holes (BH) of different sizes from stellar to galactic.

13 THE NATURE OF COLD DARK MATTER

Previous analysis on the free streaming mass, the structure formation and evolution, energy cascade, and dark matter halo density profiles strongly suggests a critical particle mass of 10^{12} GeV. This prediction is well beyond the mass range of standard thermal WIMPs but in the range of the so-called superheavy dark matter (SHDM). If the only interaction between the Standard Model and the dark sectors is gravitational, these superheavy particles have also been dubbed as

Planckian-interacting massive particles (PIDM) [1]. Except for what we discussed in this work, there are other good motives for considering such superheavy dark matter particles. Since the instability of the electroweak Higgs vacuum can also be linked to an energy scale on the same order of 10^{12} GeV [20, 27], our predicted mass scale approaches the energy scale at which new physics might emerge. Note that the prediction of such a superheavy DM mass does not rely on the details of the dark matter production mechanism. Though this scale is out of the reach of any current experiment, in this section, we can still briefly explore the possible options for the nature of the dark matter of this critical mass.

There is a wide range of possible candidates. One potential mechanism can be the production of gravitational particles in quintessential inflation [23, 31]. The nonthermal relics from gravitational production do not have to be in the local equilibrium in early universe or obey the unitarity bounds for thermal WIMPs. To have the right abundance generated during inflation, these nonthermal relics should also have a mass range between 10^{12} and 10^{16} GeV [15, 37]. The other possible superheavy dark matter candidate is the Crypton in string or M theory with a mass around 10^{12} GeV to give the right abundance [21, 4]. Detection methods for superheavy dark matter have also been discussed in the literature [11, 7].

Another interesting option can be superheavy sterile neutrinos (or heavy neutral leptons) [68]. Such right-handed neutrinos can have a ‘‘Majorana mass’’ term that is not related to the Higgs field. This seems like a very attractive option from ‘‘Occam’s razor’’ viewpoint: one tries to minimize the number of assumptions introduced but maximize the number of problems that can be addressed simultaneously. The minimal assumption we make is the existence of superheavy sterile neutrinos with a mass around 10^{12} GeV. From the seesaw mechanism and without any fine-tuning, the Yukawa couplings of these superheavy sterile neutrinos should be of the order of one to obtain the correct active sub-eV (left-handed) neutrino mass [68]. In addition, the baryon asymmetry of the Universe can also be realized through thermal leptogenesis [26]. In principle, the existence of such superheavy sterile neutrinos of mass 10^{12} GeV can account for neutrino oscillations, dark matter, and baryon asymmetry at the same time and potentially stabilizes the electroweak vacuum. In addition, axion-like dark radiation associated with these particles might also be helpful in solving the strong CP problem (Section 14).

Instead of decaying into SM particles such as (anti-) protons, neutrons, and photons, here we consider a slow instanton-induced decay process, where X particles decay into a dark radiation field with an energy on the order of $E_X \approx 10^{-9}$ eV (Eq. (122)). In this scenario, the lifetime required for a complete decay of a single X particle can be estimated both from [1] and from this work as

$$\tau_X = \frac{\hbar e^{4\pi/\alpha_X}}{m_X c^2} \quad \text{and} \quad \tau_X = \frac{m_X c^2}{\mu_X} = -\frac{c^2}{\varepsilon_u}, \quad (124)$$

where the α_X is the reduced coupling constant of the hidden gauge interaction and $\varepsilon_u \approx -10^{-7} m^2/s^3$ is the rate of energy cascade. The lifetime $\tau_X \approx 2 \times 10^{23} s = 6.2 \times 10^{15}$ yrs is much greater than the age of our universe. By equating two expressions, the coupling constant of this scenario is estimated to be $\alpha_X \approx 4\pi/137 \approx 0.092$ from Eq. (124) that is in good agreement with the prediction of α_X in [1].

14 AXION-LIKE DARK RADIATION

In this section, in analogy to the phonon radiation in superfluid turbulence with vanishingly small viscosity [76], dark radiation is postulated for collisionless dark matter flow. As the binding energy

of the smallest two-particle halo structures (Eq. (55)), the energy scale $E_X \approx (\varepsilon_u^5 \hbar^7 G^{-2})^{1/9} = 10^{-9}$ eV (Eq. (122)) strongly suggests the existence of a dark radiation field that is coupled to the X particles of mass 10^{12} GeV. This dark ‘‘radiation’’ may originate from the non-relativistic dark matter particles migrating in a non-uniform gravitational potential in haloes [79], which is produced along with the halo structure formation and evolution. The rate of energy produced as dark radiation should balance the total energy cascaded to the smallest scale (the X scale in Fig. 25) at a rate of $-0.4\varepsilon_u$. This is the sum of the rate of the energy cascade for the kinetic energy at a rate of ε_u and the potential energy at a rate of $-1.4\varepsilon_u$ from the energy evolution of the N-body system (Eq. (88)).

Although the nature of this dark ‘‘radiation’’ is not yet clear, it should be produced around the time $t_X \approx 10^{-6} s$ (Eq. (119)), during the QCD phase transition or the quark epoch, as soon as the earliest and smallest structures (two-particle haloes) formed. The mass of dark ‘‘radiation’’ is on the order of the energy scale $E_X \sim 10^{-9}$ eV (Eq. (122)) and satisfies the uncertainty principle $t_X E_X \approx \hbar$. Or equivalently, the mass should be only obtained when the Hubble rate is sufficiently small and below that mass. The formation of halo structure at the predicted time $t_X \approx 10^{-6} s$ hints at symmetry breaking and mass generation during the QCD phase transition [13]. These properties suggest that the axion may be a very promising candidate due to its small mass and weak interaction with Standard Model particles [46, 44]. In this section, we will take the axion as a candidate and estimate its properties.

If the axion is the candidate for dark ‘‘radiation,’’ it should have a mass on the order of $m_a \sim E_X = 10^{-9}$ eV. Since the axion mass is closely related to the decay constant f_a according to equation [13],

$$m_a = (5.70 \pm 0.007) \times 10^{-6} \text{eV} \left(\frac{10^{12} \text{GeV}}{f_a} \right). \quad (125)$$

This leads to a GUT (grand unification energy) energy scale at which the Peccei-Quinn (PQ) symmetry is spontaneously broken, i.e., $f_a \approx 6.5 \times 10^{15}$ GeV. The axion particle with these properties should gain its mass at a critical temperature of $T_1 \approx 230$ MeV during the quark epoch, corresponding to the time of $t_X = 10^{-6} s$. The coupling of the QCD axion to SM particles is inversely proportional to f_a , leading to an extremely weak coupling to photons with an effective coupling constant $g_{a\gamma\gamma} \sim 10^{-18} \text{GeV}^{-1}$. This is beyond the range of the current direct search for the axion [67] but should be covered within the next decade.

The energy density of dark ‘‘radiation’’ should be related to $\rho_{\text{DM}} \varepsilon_u t_0$, where ρ_{DM} is today’s dark matter density. The abundance of axion-like dark ‘‘radiation’’ ($\Omega_a h^2$) can be estimated as

$$\frac{\Omega_a h^2}{\Omega_{\text{dm}} h^2} = \frac{\varepsilon_u t_0}{c^2} = 2.2 \times 10^{-6}, \quad (126)$$

where $\Omega_{\text{dm}} h^2 = 0.119$ is the dark matter density parameter [62]. From this, the dark radiation should have a density of $\Omega_a h^2 \approx 2.6 \times 10^{-7}$, which is about 1% of the photon energy in the CMB ($\Omega_\gamma h^2 \approx 2.5 \times 10^{-5}$). The abundance of relativistic dark radiation can also be parameterized by increasing the effective number of neutrino species [32]. That increase in the present epoch is given by

$$\Delta N_{\text{eff}} = \frac{8}{7} \left(\frac{11}{4} \right)^{1/3} \frac{\Omega_a h^2}{\Omega_\gamma h^2} \approx 0.02. \quad (127)$$

Dark radiation was proposed to alleviate disagreements about the current expansion rate H_0 and the amplitude of matter fluctuation S_8 between the prediction of the model Λ CDM and direct measurements in the local universe, namely the Hubble tension and the S_8 tension

Table 5. Physical scales for cold collisionless and self-interacting dark matter

Scales	Fully collisionless	Self-interacting
Length	$l_X = (-G\hbar/\varepsilon_u)^{1/3}$	$r_\eta = \varepsilon_u^2 G^{-3} (\sigma/m)^3$
Time	$t_X = (-G^2\hbar^2/\varepsilon_u^5)^{1/9}$	$t_\eta = -\varepsilon_u G^{-2} (\sigma/m)^2$
Mass	$m_X = (-\varepsilon_u\hbar^5/G^4)^{1/9}$	$m_\eta = \varepsilon_u^4 G^{-6} (\sigma/m)^5$
Density	$\rho_X = (\varepsilon_u^{10}\hbar^{-4}/G^{13})^{1/9}$	$\rho_\eta = \varepsilon_u^{-2} G^3 (\sigma/m)^{-4}$

[57, 14]. With dark matter and axion dark "radiation" presented in this work, more study is still required for their effects on cosmological observations and disagreements.

15 SELF-INTERACTING DARK MATTER

Note that the particle mass m_X is only weakly dependent on ε_u as $m_X \propto \varepsilon_u^{1/9}$ (Eq. (118)) such that the estimation of m_X should be fairly robust for a wide range of possible values of ε_u . A small change in m_X requires a large change in ε_u . Unless gravity is not the only interaction, the uncertainty in the predicted m_X should be small. In other words, if our estimate (ε_u in Eq. (89)) is accurate and gravity is the only interaction on the smallest scale, it seems implausible for dark matter particles with any mass far above 10^{12}GeV to produce the given value of the energy cascade rate $\varepsilon_u \approx 10^{-7}m^2/s^3$. If the mass of dark matter particles has a different value, there might be some new interactions beyond gravity. This can be the self-interacting dark matter (SIDM) model as a potential solution for the "cusp-core" problem [70].

For self-interacting dark matter, a key parameter is the cross-section σ/m (in the unit: m^2/kg) of self-interaction that can be constrained by various astrophysical observations. Self-interaction introduces an additional scale, below which self-interaction is dominant over gravity to suppress all small-scale structures, and the scaling laws for dark matter haloes in Section 11 are no longer valid. In this case, the dark matter particle properties can be obtained only if the nature and dominant constants of self-interaction are known. Three constants determine the smallest scale for the existence of a halo structure, that is, the rate of the energy cascade ε_u , the gravitational constant G , and the cross-section σ/m . In other words, the cross-section might be estimated if the scale of the smallest structure is known. Table 5 lists the relevant scales for both collisionless and self-interacting dark matter. Taking the value of $\sigma/m = 0.01m^2/kg$ used for the cosmological SIDM simulation to reproduce the right halo core size and central density [64], these scales are also plotted in Fig. 23. More insights can be obtained by extending the current analysis to self-interacting dark matter simulations.

16 CONCLUSIONS

In this paper, we have discussed the formation and evolution of nonlinear halo structures in different eras. A critical mass scale m_{Xc} is identified on the order of 10^{12}GeV . Dark matter particles seem to prefer to have a mass of that critical mass because i) particles of this mass can form the smallest possible structure (Fig. 2); ii) particles of this mass can have a direct collision time comparable to the formation time. This allows for the formation of the smallest and earliest two-particle haloes by direct collisions (Eq. (54)); iii) particles of this mass have the shortest possible waiting time to allow for the formation of haloes observed today as large as $10^{13}M_\odot$ (Eq.

(67)). Particles smaller than m_{Xc} will not have enough time to grow haloes of that size. In particular, iv) particles of this mass give rise to the key parameter ε_u (Eq. (56)) that influences the halo dynamics and density profiles, which is consistent with N-body simulations and observations. The rapid growth of halo structures in the radiation and matter eras eventually slows down due to the self-limiting effects of dark energy in the dark energy era (Table 2).

We identified the mass and energy cascade for the cold and collisionless dark matter within the ΛCDM cosmology, which operates in all eras. The concept was demonstrated by Illustris simulations. The energy cascade leads to a two-thirds law for kinetic energy or, equivalently, to five-thirds and four-thirds laws for halo mass and halo density (Eq. (104)). All scaling laws can be confirmed by cosmological N-body simulations and galaxy rotation curves. For collisionless dark matter, viscosity is not present, and gravity is the only interaction such that the established scaling laws on halo scales can be extended to the smallest scale, where quantum effects become important. The dominant constants on that scale include the rate of the energy cascade ε_u , the Planck constant \hbar , and the gravitational constant G . Cold dark matter particles were proposed to have a mass $m_X = (\varepsilon_u\hbar^5G^{-4})^{1/9} = 0.9 \times 10^{12}\text{GeV}$, a size $l_X = (\varepsilon_u^{-1}\hbar G)^{1/3} = 3 \times 10^{-13}\text{m}$, and a characteristic time of $\tau_X = c^2/\varepsilon_u = 10^{16}$ years, along with other important properties. Heavy dark matter particles of this mass were shown to have a free streaming mass comparable to its particle mass. This allows us to extend the scaling laws to the mass scale of individual dark matter particles. The potential extension to self-interacting dark matter was also discussed with relevant scales estimated for a given cross-section σ/m (see Table 5). The binding energy $E_X = (\varepsilon_u^5\hbar^7G^{-2})^{1/9} = 10^{-9}\text{eV}$ suggests a dark "radiation" field. If the axion is the dark "radiation," it should have a mass 10^{-9}eV with a GUT scale decay constant 10^{16}GeV and an effective axion-photon coupling constant 10^{-18}GeV^{-1} . This work suggests a heavy dark matter scenario with a mass much larger than that of WIMPs and an axion-like dark radiation associated with the structure formation and evolution.

ACKNOWLEDGEMENTS

This research was supported by Laboratory Directed Research and Development at Pacific Northwest National Laboratory (PNNL). PNNL is a multiprogram national laboratory operated for the U.S. Department of Energy (DOE) by Battelle Memorial Institute under contract no. DE-AC05-76RL01830.

DATA AVAILABILITY

Two datasets for this article, that is, halo-based and correlation-based statistics of dark matter flow, are available on Zenodo [83, 84], along with the accompanying presentation "A comparative study of dark matter flow & hydrodynamic turbulence and its applications" [81]. All data are also available on GitHub [82].

References

- [1] Abreu P., et al., 2023, *Phys. Rev. D*, 107, 042002
- [2] Adams J. J., et al., 2014, *ApJ*, 789, 63
- [3] Aghanim N., et al., 2021, *Astronomy & Astrophysics*, 652
- [4] Benakli K., Ellis J., Nanopoulos D. V., 1999, *Phys. Rev. D*, 59, 047301

- [5] Bertschinger E., 2006, *Phys. Rev. D*, 74, 063509
- [6] Blanco C., Delos M. S., Erickcek A. L., Hooper D., 2019, *Phys. Rev. D*, 100, 103010
- [7] Blanco C., Elshimy B., Lang R. F., Orlando R., 2022, *Physical Review D*, 105
- [8] Boylan-Kolchin M., Bullock J. S., Kaplinghat M., 2011, *Monthly Notices of the Royal Astronomical Society: Letters*, 415, L40
- [9] Boylan-Kolchin M., Bullock J. S., Kaplinghat M., 2012, *Monthly Notices of the Royal Astronomical Society*, 422, 1203
- [10] Bullock J. S., Boylan-Kolchin M., 2017, *ARA&A*, 55, 343
- [11] Carney D., et al., 2022, Snowmass2021 Cosmic Frontier White Paper: Ultraheavy particle dark matter, doi:10.48550/ARXIV.2203.06508, <https://arxiv.org/abs/2203.06508>
- [12] Castellano M., et al., 2022, *The Astrophysical Journal Letters*, 938, L15
- [13] Chadha-Day F., Ellis J., Marsh D. J. E., 2022, *Science Advances*, 8, eabj3618
- [14] Chen A., et al., 2021, *Phys. Rev. D*, 103, 123528
- [15] Chung D. J. H., Kolb E. W., Riotto A., 1999, *Physical Review D*, 59
- [16] Cooray A., Sheth R., 2002, *Physics Reports-Review Section of Physics Letters*, 372, 1
- [17] Del Popolo A., Le Delliou M., 2017, *Galaxies*, 5, 17
- [18] Diemand J., Moore B., 2011, *Advanced Science Letters*, 4, 297
- [19] Duffy L. D., van Bibber K., 2009, *New Journal of Physics*, 11, 105008
- [20] Eichhorn A., Gies H., Jaeckel J., Plehn T., Scherer M. M., Sondenheimer R., 2015, *JHEP*, 04, 022
- [21] Ellis J., Lopez J. L., Nanopoulos D. V., 1990, *Physics Letters B*, 247, 257
- [22] Flores R. A., Primack J. R., 1994, *ApJ*, 427, L1
- [23] Ford L. H., 1987, *Phys. Rev. D*, 35, 2955
- [24] Frenk C. S., White S. D. M., 2012, *Annalen der Physik*, 524, 507
- [25] Frenk C. S., et al., 2000, [arXiv:astro-ph/0007362v1](https://arxiv.org/abs/astro-ph/0007362v1)
- [26] Fukugita M., Yanagida T., 1986, *Phys. Lett. B*, 174, 45
- [27] Goswami G., Mohanty S., 2015, *Phys. Lett. B*, 751, 113
- [28] Governato F., et al., 2010, *Nature*, 463, 203
- [29] Griest K., Kamionkowski M., 1990, *Physical Review Letters*, 64, 615
- [30] Gunn J. E., Gott J. R., 1972, *Astrophysical Journal*, 176, 1
- [31] Haro J., Saló L. A., 2019, *Phys. Rev. D*, 100, 043519
- [32] Higaki T., Nakayama K., Takahashi F., 2013, *Journal of Cosmology and Astroparticle Physics*, 2013, 030
- [33] Irvine W. M., 1961, Thesis, HARVARD UNIVERSITY
- [34] Jenkins A., et al., 1998, *Astrophysical Journal*, 499, 20
- [35] Jungman G., Kamionkowski M., Griest K., 1996, *Physics Reports-Review Section of Physics Letters*, 267, 195
- [36] Klypin A., Kravtsov A. V., Valenzuela O., Prada F., 1999, *The Astrophysical Journal*, 522, 82
- [37] Kolb E. W., Long A. J., 2017, *Physical Review D*, 96
- [38] Kolmogoroff A. N., 1941, *Comptes Rendus De L Academie Des Sciences De L Urss*, 32, 16
- [39] Komatsu E., et al., 2011, *ApJS*, 192, 18
- [40] Layzer D., 1963, *Astrophysical Journal*, 138, 174
- [41] Lelli F., McGaugh S. S., Schombert J. M., 2016, *AJ*, 152, 157
- [42] Li P., Lelli F., McGaugh S., Schombert J., 2020, *ApJS*, 247, 31
- [43] Lovell M. R., et al., 2012, *Monthly Notices of the Royal Astronomical Society*, 420, 2318
- [44] Marsh D. J. E., 2016, *Phys. Rep.*, 643, 1
- [45] Martinsson T. P. K., Verheijen M. A. W., Westfall K. B., Bershadsky M. A., Andersen D. R., Swaters R. A., 2013, *A&A*, 557, A131
- [46] Mazumdar A., Qutub S., Saikawa K., 2016, *Phys. Rev. D*, 94, 065030
- [47] McKeown D., et al., 2022, *MNRAS*, 513, 55
- [48] Meszaros P., 1974, *A&A*, 37, 225
- [49] Mo H. J., White S. D. M., 2002, *MNRAS*, 336, 112
- [50] Mo H., van den Bosch F., White S., 2010, *Galaxy formation and evolution*. Cambridge University Press, Cambridge
- [51] Moore B., Ghigna S., Governato F., Lake G., Quinn T., Stadel J., Tozzi P., 1999, *The Astrophysical Journal*, 524, L19
- [52] Navarro J. F., Frenk C. S., White S. D. M., 1997, *Astrophysical Journal*, 490, 493
- [53] Navarro J. F., et al., 2010, *Monthly Notices of the Royal Astronomical Society*, 402, 21
- [54] Nelson D., et al., 2015, *Astronomy and Computing*, 13, 12
- [55] Neyman J., Scott E. L., 1952, *Astrophysical Journal*, 116, 144
- [56] Oman K. A., et al., 2015, *Monthly Notices of the Royal Astronomical Society*, 452, 3650
- [57] Pandey K. L., Karwal T., Das S., 2020, *Journal of Cosmology and Astroparticle Physics*, 2020, 026
- [58] Peebles P. J. E., 1980, *The Large-Scale Structure of the Universe*. Princeton University Press, Princeton, NJ
- [59] Peebles P. J. E., 1982, *ApJ*, 263, L1
- [60] Peebles P. J. E., 1984, *ApJ*, 284, 439
- [61] Perivolaropoulos L., Skara F., 2022, *New Astronomy Reviews*, 95, 101659
- [62] Planck Collaboration et al., 2014, *A&A*, 571, A16
- [63] Richardson L. F., 1922, *Weather Prediction by Numerical Process*. Cambridge University Press, Cambridge, UK
- [64] Rocha M., Peter A. H. G., Bullock J. S., Kaplinghat M., Garrison-Kimmel S., Oñorbe J., Moustakas L. A., 2013, *Monthly Notices of the Royal Astronomical Society*, 430, 81
- [65] Rubin V. C., Ford W. K., 1970, *Astrophysical Journal*, 159, 379
- [66] Rubin V. C., Ford W. K., Thonnard N., 1980, *Astrophysical Journal*, 238, 471
- [67] Semertzidis Y. K., Youn S., 2022, *Science Advances*, 8, eabm9928
- [68] Shaposhnikov M., 2024, *Nuclear Physics B*, 1003, 116496
- [69] Sofue Y., 2016, *Publications of the Astronomical Society of Japan*, 68
- [70] Spergel D. N., Steinhardt P. J., 2000, *Phys. Rev. Lett.*, 84, 3760
- [71] Spergel D. N., et al., 2003, *ApJS*, 148, 175
- [72] Steigman G., Turner M. S., 1985, *Nuclear Physics B*, 253, 375
- [73] Tulin S., Yu H.-B., 2018, *Physics Reports*, 730, 1
- [74] Viel M., Lesgourgues J., Haehnelt M. G., Matarrese S., Riotto A., 2005, *Phys. Rev. D*, 71, 063534
- [75] Viel M., Becker G. D., Bolton J. S., Haehnelt M. G., 2013, *Phys. Rev. D*, 88, 043502
- [76] Vinen W. F., 2001, *Phys. Rev. B*, 64, 134520
- [77] Wang J., Bose S., Frenk C. S., Gao L., Jenkins A., Springel V., White S. D. M., 2020, *Nature*, 585, 39
- [78] Weinberg D. H., Bullock J. S., Governato F., de Naray R. K., Peter A. H. G., 2015, *Proceedings of the National Academy of Sciences*, 112, 12249
- [79] Xu Z., 2021a, *arXiv e-prints*, p. arXiv:2109.09985
- [80] Xu Z., 2021b, *arXiv e-prints*, p. arXiv:2110.05784
- [81] Xu Z., 2022c, A comparative study of dark mat-

- ter flow & hydrodynamic turbulence and its applications, doi:10.5281/zenodo.6569901, <http://dx.doi.org/10.5281/zenodo.6569901>
- [82] Xu Z., 2022d, Dark matter flow dataset, doi:10.5281/zenodo.6586212, https://github.com/ZhijieXu2022/dark_matter_flow_dataset
- [83] Xu Z., 2022a, Dark matter flow dataset Part I: Halo-based statistics from cosmological N-body simulation, doi:10.5281/zenodo.6541230, <http://dx.doi.org/10.5281/zenodo.6541230>
- [84] Xu Z., 2022b, Dark matter flow dataset Part II: Correlation-based statistics from cosmological N-body simulation, doi:10.5281/zenodo.6569898, <http://dx.doi.org/10.5281/zenodo.6569898>
- [85] Xu Z., 2022e, [arXiv e-prints](https://arxiv.org/abs/2202.04054), p. arXiv:2202.04054
- [86] Xu Z., 2023a, [Scientific Reports](https://doi.org/10.1038/s41598-023-28165-1), 13, 4165
- [87] Xu Z., 2023b, [Scientific Reports](https://doi.org/10.1038/s41598-023-28165-1), 13, 16531
- [88] Xu Z., 2023c, [Physics of Fluids](https://doi.org/10.1038/s41598-023-28165-1), 35, 077105
- [89] Xu Z., 2023d, [A&A](https://doi.org/10.1051/0004-6361/202346759), 675, A92
- [90] Xu Z., 2024, [Research Square](https://doi.org/10.21961/RS.2024.13.1)
- [91] de Blok W. J. G., 2010, [Adv. Astron.](https://doi.org/10.1086/505093), 2010, 789293